AFRL-AFOSR-UK-TR-2021-0013

Damage Tolerance and Durability of Structural Power Composites

Asp, Leif
CHALMERS TEKNISKA HOGSKOLA AB
CHALMERSPLATSEN 4
GOTEBORG, , 41296
SWE

06/21/2021
Final Technical Report

Air Force Research Laboratory
Air Force Office of Scientific Research
European Office of Aerospace Research and Development
Unit 4515 Box 14, APO AE 09421

REPORT DOCUMENTATION PAGE	*Form Approved* *OMB No. 0704-0188*

The public reporting burden for this collection of information is estimated to average 1 hour per response, including the time for reviewing instructions, searching existing data sources, gathering and maintaining the data needed, and completing and reviewing the collection of information. Send comments regarding this burden estimate or any other aspect of this collection of information, including suggestions for reducing the burden, to Department of Defense, Washington Headquarters Services, Directorate for Information Operations and Reports (0704-0188), 1215 Jefferson Davis Highway, Suite 1204, Arlington, VA 22202-4302. Respondents should be aware that notwithstanding any other provision of law, no person shall be subject to any penalty for failing to comply with a collection of information if it does not display a currently valid OMB control number.
PLEASE DO NOT RETURN YOUR FORM TO THE ABOVE ADDRESS.

1. REPORT DATE *(DD-MM-YYYY)* 21-06-2021	**2. REPORT TYPE** Final	**3. DATES COVERED** *(From - To)* 30 Sep 2017 - 29 Sep 2020

4. TITLE AND SUBTITLE Damage Tolerance and Durability of Structural Power Composites	**5a. CONTRACT NUMBER**
	5b. GRANT NUMBER FA9550-17-1-0338
	5c. PROGRAM ELEMENT NUMBER
6. AUTHOR(S) Leif Asp	**5d. PROJECT NUMBER**
	5e. TASK NUMBER
	5f. WORK UNIT NUMBER
7. PERFORMING ORGANIZATION NAME(S) AND ADDRESS(ES) CHALMERS TEKNISKA HOGSKOLA AB CHALMERSPLATSEN 4 GOTEBORG, 41296 SWE	**8. PERFORMING ORGANIZATION REPORT NUMBER**
9. SPONSORING/MONITORING AGENCY NAME(S) AND ADDRESS(ES) EOARD UNIT 4515 APO AE 09421-4515	**10. SPONSOR/MONITOR'S ACRONYM(S)** AFRL/AFOSR IOE
	11. SPONSOR/MONITOR'S REPORT NUMBER(S) AFRL-AFOSR-UK-TR-2021-0013

12. DISTRIBUTION/AVAILABILITY STATEMENT
A Distribution Unlimited: PB Public Release

13. SUPPLEMENTARY NOTES

14. ABSTRACT
Research objective successfully met; deliverables received.

15. SUBJECT TERMS

16. SECURITY CLASSIFICATION OF:			**17. LIMITATION OF ABSTRACT**	**18. NUMBER OF PAGES**	**19a. NAME OF RESPONSIBLE PERSON** DAVID GARNER
a. REPORT	**b. ABSTRACT**	**c. THIS PAGE**			**19b. TELEPHONE NUMBER** *(Include area code)* 314-235-6420
U	U	U	SAR	32	

Standard Form 298 (Rev.8/98)
Prescribed by ANSI Std. Z39.18

Final Technical report

Damage Tolerance and Durability of Structural Power Composites, Award FA9550-17-1-0338

This is a technical report on the work performed at Chalmers University of Technology, Gothenburg, Sweden under the award no. FA9550-17-1-0338 during the time period 2017-10-01 to 2020-09-30. It is intentionally brief and only covers short descriptions of the work performed that has resulted in publications. The journal publications are appended to this report.

The work is focused on structural battery composites and their constituents. The work performed is divided in three areas: Multiphysics model development; characterisation of material properties of the structural battery composite and its constituents; and realisation of the structural battery full cell and implications thereof.

Design and analysis of structural battery composites require access to Multiphysics models. For this purpose, a computational framework that considers the coupled electro-chemo-mechanical processes in a structural battery has been developed. Input data for such models are vast and we have taken on the challenge to characterise some of the more fundamental material properties. Finally, we build and characterise the multifunctional performance of a structural battery full cell. The structural battery composite demonstrates unprecedented multifunctional properties. Some more in-depth descriptions of this work are presented below.

All-in-all the work has resulted in 11 journal papers and 5 conference papers completely or partly funded by this AFOSR/EOARD grant. Some of the work has been done in collaboration with The Royal Institute of Technology, KTH,) with Prof. Dan Zenkert and his team.

The Team

This project has been conducted as part of a larger portfolio of projects run by an interdisciplinary team at Chalmers headed by Prof. Asp. All together four Ph.D.-students and one post-doc have been involved (Figure 1).

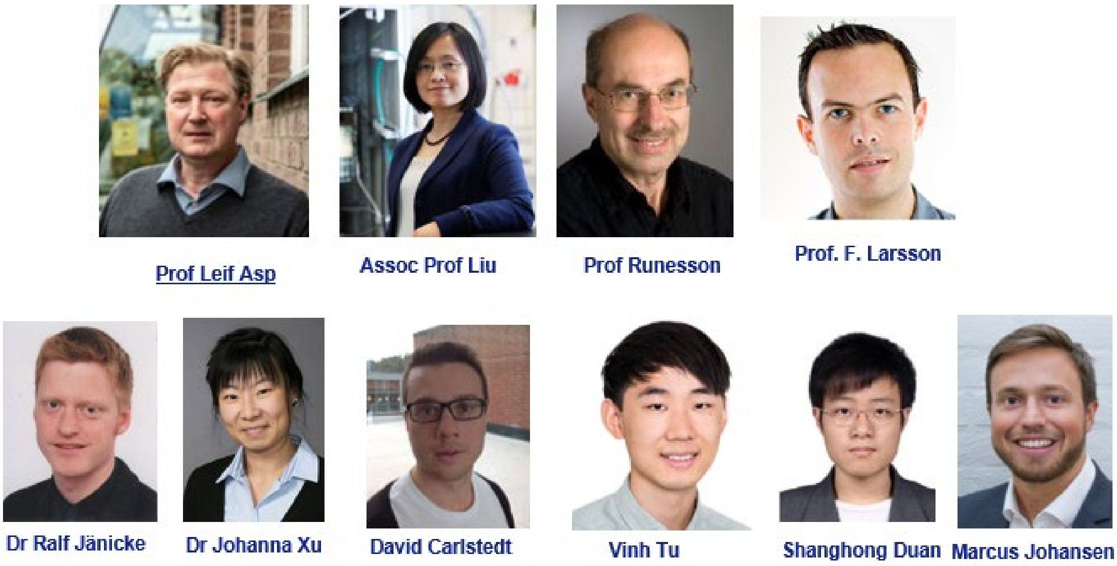

Figure 1: The structural battery research team at Chalmers in 2020.

Highlights

Highlights among the accomplishments of the Chalmers' team in the EOARD project "Damage Tolerance and Durability of Structural Power Composites":

- A general electro-chemo-mechanical computational framework for analysis and design of structural battery composites
- State-of-charge found to affect the elastic properties of the structural battery composite
- Interfacial strength between carbon fibres and the structural battery electrolyte characterised
- Joule heating of structural batteries found to occur and limits allowable dimensions of the structural battery composite cell
- A technique to measure transverse and shear moduli of single carbon fibres
- A structural positive electrode using exfoliated graphene oxide scaffolds for high lithium iron phosphate loadings
- Combined all previous research work on structural batteries in a review paper
- A structural battery concept with unprecedented multifunctional performance
- Shown that structural batteries can save mass on systems level and lead to reduced environmental impact at maintained or increased drive range for electric vehicles

Papers published in peer-reviewed journals with EOARD/AFOSR funding

Multiphysics modelling:

Carlstedt D, Marklund E, Asp LE. Effects of state of charge on elastic properties of 3D structural battery composites. *Composites Science and Technology*. **169**, 2019, pp. 26-33. https://doi.org/10.1016/j.compscitech.2018.10.033.

This is the first paper where try to model the multifunctional performance of a structural battery composite. Here we address the so-called 3D structural battery composite. The objective of the work was to investigate the effects of state-of-charge (SOC) on the elastic properties of a structural battery composite. For this purpose, a parametric study is performed. Reported achievements are: A semi-analytical model to analyse the mechanical properties of 3D structural battery composites has been developed and verified (see Figure 2). From the parametric studies the transverse elastic properties E_2 and G_{23} and the in-plane shear modulus G_{12} are found to be highly affected by the SOC for critical configurations.

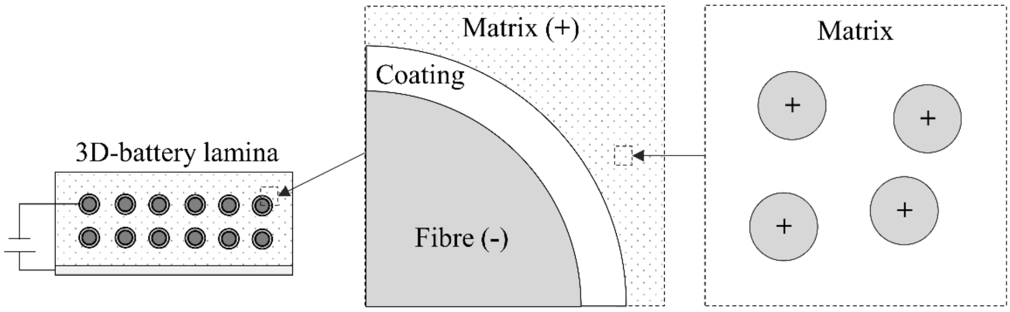

Figure 2: Effects of state-of-charge on the elastic properties of a structural battery composite.

Carlstedt D, Asp LE. Thermal and diffusion induced stresses in a structural battery under galvanostatic cycling. *Composites Science and Technology*. **179**, 2019, pp. 69-78. https://doi.org/10.1016/j.compscitech.2019.04.024.

The objective of this paper was to investigate the effects of the generated heat and expansion / shrinkage of the constituents on the internal stress state and mechanical properties of structural battery composites. For this purpose, thermo-mechanical analyses were performed considering diffusion (ion-currents) and resistive heating (electron-currents) in the structural electrolyte and carbon fibres, respectively. For the analyses, the semi-analytical model developed by Carlstedt, Marklund and Asp was employed. The generated heat was found to strongly affect the internal stress state in structural battery composites. Furthermore, the charge / discharge current, lamina dimensions and residual stresses have significant effect on the internal stress state and effective properties of the composite lamina. Effects of lamina dimensions on the generated heat and internal stress state are depicted in Figure 3.

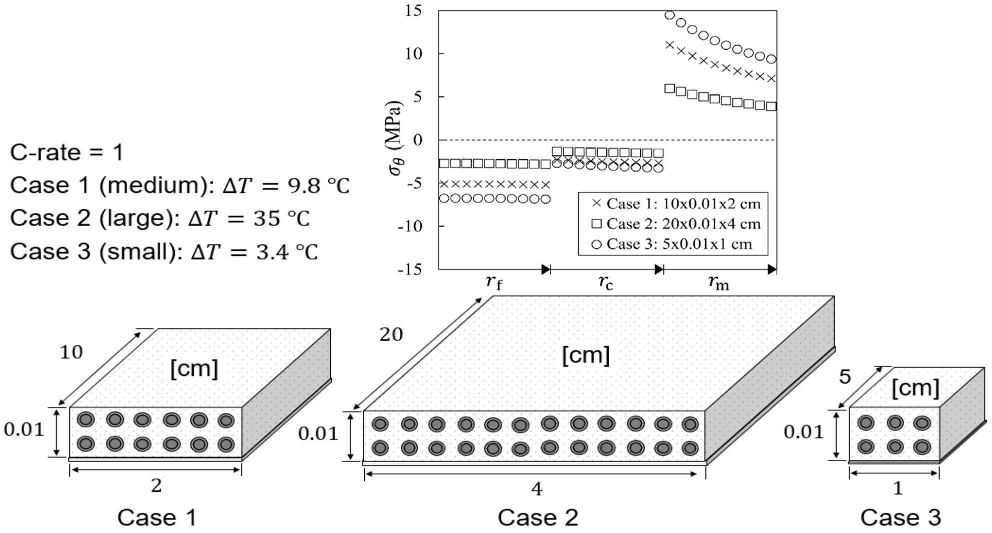

Figure 3: Effects of the structural battery dimensions on generated heat and internal stress state.

Tu V, Asp LE, Shirshova N, Larsson F, Runesson K, Jänicke R. Performance of Bicontinuous Structural Electrolytes. *Multifunctional Materials*, **3**, 2020, 025001, https://doi.org/10.1088/2399-7532/ab8d9b.

In this study we set out to develop a computational method to identify highly multifunctional Structural Battery Electrolyte (SBE) architectures. Current SBEs are synthesised without any information on the desired topology for best multifunctional performance. For this purpose, numerous bicontinuous material computational models were generated and analysed. The investigated microstructural topologies are realizable over wide porosity ranges yet forming a bicontinuous system. The computational method provides a cheap, fast and reliable way to guide polymer synthesis of bicontinuous SBEs. An illustration from the model generation, one of the model and a micrograph of the porous SBE (sub-micron pores) as well as a graph that demonstrates the trade-off between Young's modulus and ion mobility for the SBE (including the Voigt-Taylor upper bound and the experimental data) are shown in Figure 4.

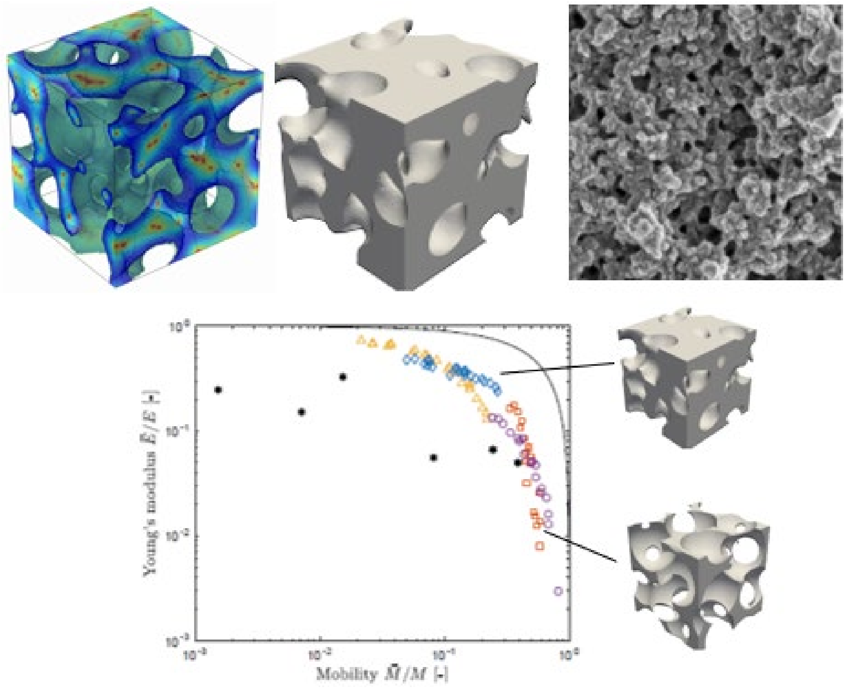

Figure 4: The bicontinuous structural battery electrolyte and examples of generated models and predicted multifunctional performance.

Carlstedt D, Runesson K, Larsson F, Xu J, Asp LE. Electro-chemo-mechanically coupled computational modelling of structural batteries. *Multifunctional Materials*, Accepted, 2020. https://doi.org/10.1088/2399-7532/abc60d.

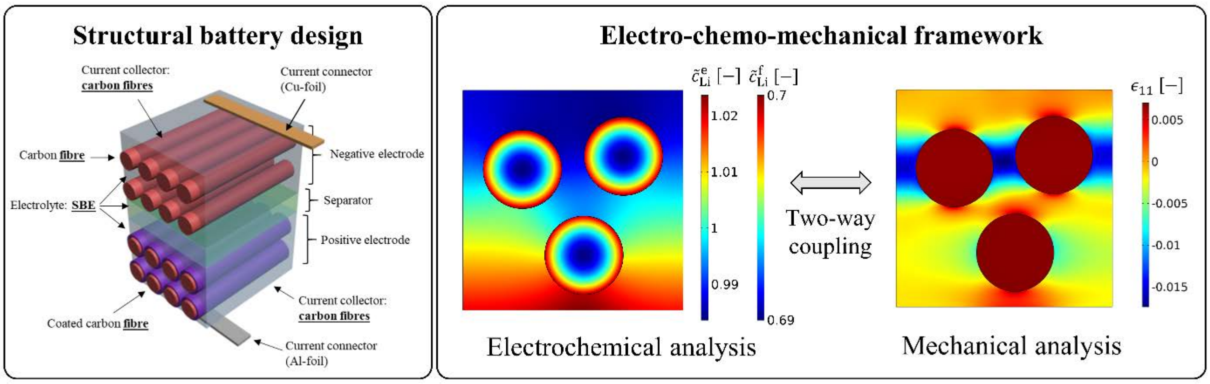

Figure 5: The structural battery and the predicted variations in Li-ion concentration and internal strains.

The objective of this paper was to develop and validate a fully electro-chemo-mechanically coupled computational model for structural batteries. Here, a thermodynamically consistent modelling approach is used. We consider effects of lithium insertion in the transversely isotropic carbon fibres, leading to insertion strains (see Figure 5). Further, stress-assisted ionic transport is accounted for in addition to standard diffusion and migration. As a proof of concept, the numerical studies reveal that it is vital to account for two-way coupling in order to predict the multifunctional (i.e. combined electro-chemo-mechanical) performance of structural batteries.

Experimental Characterisation:

Xu J, Johannisson W, Johansen M, Liu F, Zenkert D, Lindbergh G, Asp LE. Characterization of the adhesive properties between structural battery electrolytes and carbon fibers. *Composites Science and Technology*. **188**, 2020, 107962. https://doi.org/10.1016/j.compscitech.2019.107962.

This paper is devoted to studying the interface between the SBE and the carbon fibres. This interface must be multifunctional: transfer mechanical loads and be ion conductive. This leads to a trade-off between the polymer contact creating adhesion and liquid contact creating ionic conductivity (Figure 6 left). We investigated the fibre-matrix adhesion between carbon fibres with different sizing and two different SBE systems, using micro droplet testing supported (Figure 6, right) by transverse tensile tests. The results show that the mechanical adhesion of the fibre-matrix interface is lower than that of a commercial non-ion conducting polymer matrix but enough for structural battery applications.

This work was a collaboration between Chalmers and KTH.

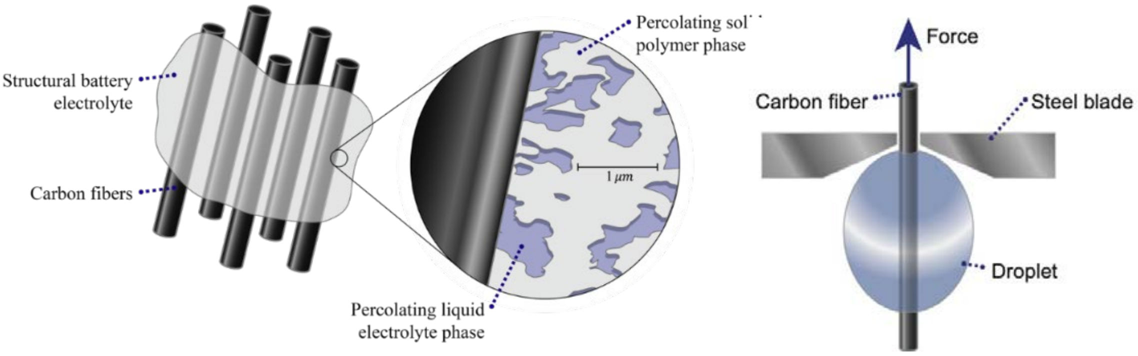

Figure 6: (left) Schematic of carbon fibres in a structural battery electrolyte. Within a structural battery, the carbon fibres are included in a structural battery electrolyte. This matrix material both transfer load between the reinforcing fibres using a percolating network of solid polymer, and conduct lithium ions through a network of liquid electrolyte. (right) The micro droplet test set-up.

Schutzeichel MOH, Kletschkowski T, Linde P, Asp LE. Experimental characterization of multifunctional polymer electrolyte coated carbon fibres, *Functional Composites and Structures*. **1**, 2019, 025001. https://doi.org/ 10.1088/2631-6331/ab136b.

In this paper we collaborated with the University of Applied Sciences in Hamburg and Airbus to investigate the solid polymer electrolyte (SPE) coating durability on carbon fibres, the longitudinal electrical conductivity of unsized IMS65 carbon fibres and their thermo-electrical coupling (Joule heating). Ohmic resistivity of the fibres was proven (see Figure 7). A temperature independent ohmic longitudinal resistance of the coated carbon fibre electrode was demonstrated, lying at the lower end of semi-conductors. This is beneficial, since Joule heating and resulting temperatures can be predicted based on a temperature independent resistor. Temperature prediction is necessary to control/predict the mechanical behaviour of the structural battery as shown by Carlstedt and Asp (2019). In the current paper, a method to determine the number of carbon fibres in an electrode, based on resistance measurements, was also demonstrated.

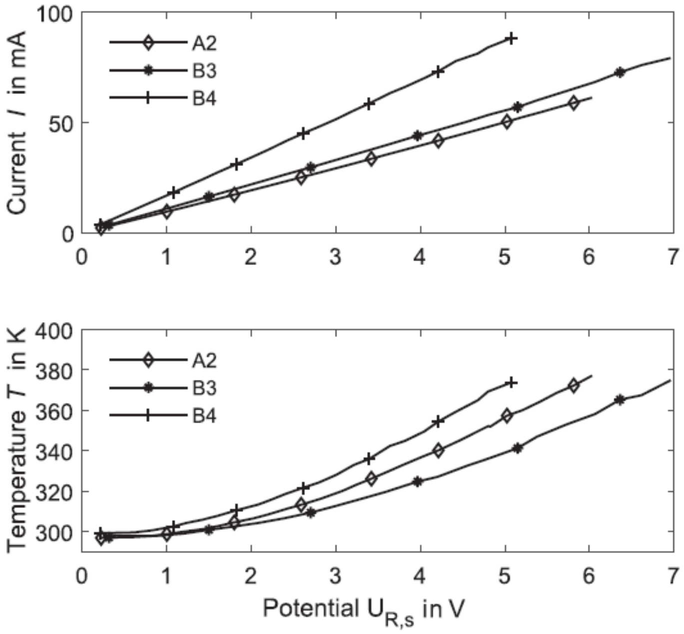

Figure 7: Current versus potential and temperature versus potential curves for SPE coated carbon fibre electrodes.

Duan S, Liu F, Pettersson T, Creighton C, Asp LE. Determination of transverse and shear moduli of single carbon fibres. *Carbon*. **158C**, 2020, 772-782. https://doi.org/10.1016/j.carbon.2019.11.054.

It has been shown that the out-of-plane modulus for graphite is increased almost three times on lithium atoms insertion. Consequently, one can expect the modulus in the radial direction of a carbon fibre to increase as lithium is inserted. This paper presents a study with the objective to determine the longitudinal, transverse and shear moduli of single carbon fibres. There is currently no such method available. Here, we developed a method where we use FIB/SEM to produce flat surfaces for indentation tests using AFM. As a result, E_l, E_t, G_{lt} determined for T800, IMS65 and M60J fibres (see Figure 8). Equipped with these methods and data we can proceed to investigate effects from lithium insertion on these mechanical properties. This work was done in collaboration with Deakin University, Australia, and KTH.

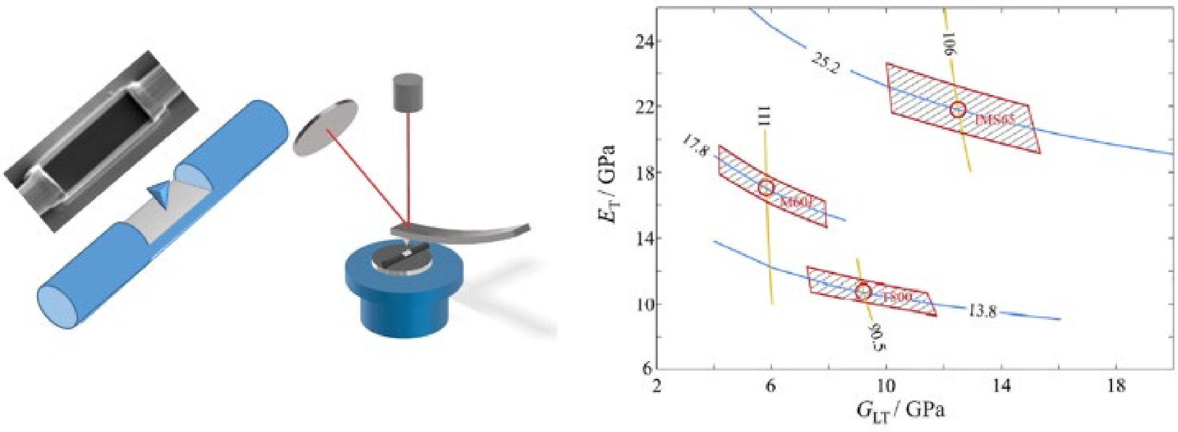

Figure 8: Indentation tests using AFM and the measured transverse and shear moduli of carbon fibres.

Sanchez JS, Xu J, Xia Z, Sun J, Asp LE, Palermo V. Electrophoretic coating of LiFePO4/Graphene oxide on Carbon Fibres as High-Performance Cathode Electrodes for Structural Lithium Ion Batteries. Submitted, 2020.

The first-generation structural battery composite utilizes a commercial positive electrode foil. To date, no carbon fibre reinforced positive electrode with sufficiently high lithium phosphate (LFP) content has been made. In this paper we develop a binder-free method to deposit a composite of LFP and electrochemically exfoliated graphene oxide (EGO) on to carbon fibres. We use electrophoretic deposition as a versatile, scalable and cost-effective technique to deposit uniform coatings on substrates with complex shapes, as schematically illustrated in Figure 9. Tests performed on full cells with pristine CF as anode demonstrate: Specific energy density of 168.8 Wh kg^{-1}; Power density of 1.5 kW kg^{-1}; 80% capacity retention at 1 C over 300 cycles.

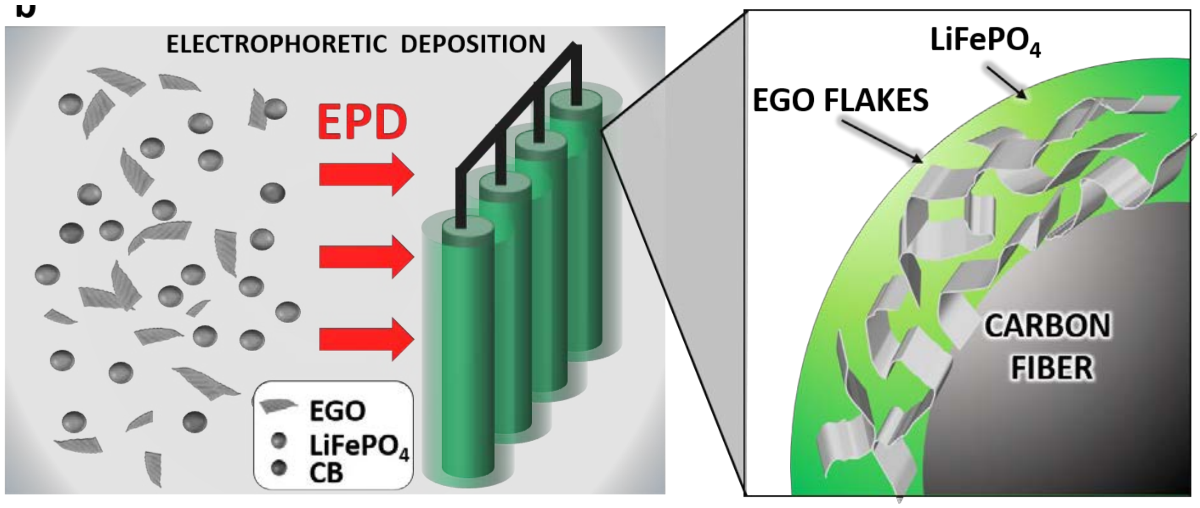

Figure 9: Schematic illustration of the electrophoretic deposition of LFP EGO coatings on carbon fibre reinforced positive electrodes.

<u>Structural battery composites:</u>

Asp LE, Johansson M, Lindbergh G, Xu J, Zenkert D. Structural Battery Composites: A Review, *Functional Composites and Structures*, **1**, 2019, 042001. https://dx.doi.org/10.1088/2631-6331/ab5571.

In this paper we provide an overview of research performed on structural battery composites to date. The conceptual idea is shown in Figure 10. Substantial work has been performed. However, significant work on the structural battery full cell and its manufacture and validation remains before structural battery composites offer a solution for mass-less energy storage in future electric road, air and sea transport applications. To date, no showstoppers for the realisation of structural battery composites have been identified.

This work was a collaboration between Chalmers and KTH.

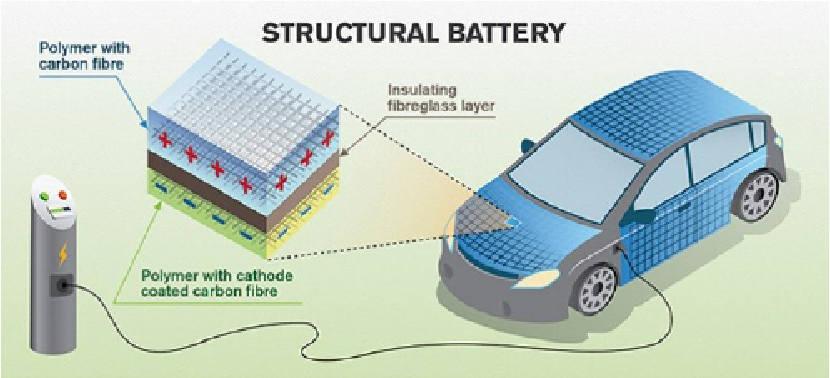

Figure 10: The concept of structural batteries, a material that carries loads and stores energy simultaneously.

Carlstedt D, Asp LE. Performance analysis framework for structural battery composites in electric vehicles. *Composites Part B*, **186**, 2020, 107822. https://doi.org/10.1016/j.compositesb.2020.107822.

The objective of this paper was to develop a modelling framework to estimate system level performance of EVs using a structural battery composite material. Electrical and mechanical properties are derived from material data of the constituents, device design and connection / layup schemes. System weight reductions are predicated for different amount of structural batteries introduced in BMW i3 and Tesla Model S. Knowledge of the multifunctional, i.e. electrical and mechanical, performance of the structural battery composite allows for estimation of drive range for any known drive cycle. Predictions for the New European Drive Cycle (NEDC), illustrated to the left in Figure 11, are presented for different cases to the right in Figure 11.

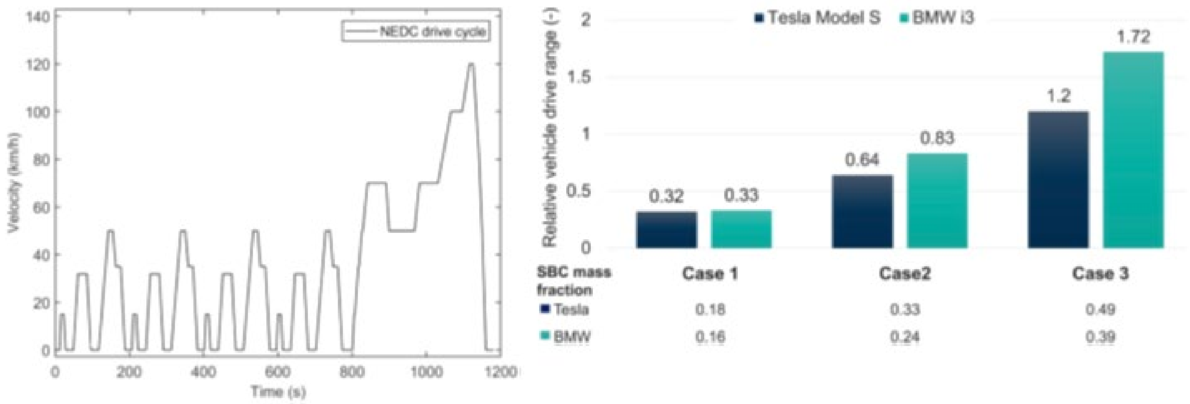

Figure 11: The New European Drive Cycle and predicted drive range replacing traditional batteries with structural batteries in BMW i3 and Tesla Model S electric vehicles.

Asp LE, Bouton K, Carlstedt D, Duan S, Harnden R, Johannisson W, Johansen M, Johansson MKG, Lindbergh G, Liu F, Peuvot K, Schneider LM, Xu J, Zenkert D. A structural battery and its multifunctional performance. Submitted, 2020.

Engineering materials that can store electrical energy in structural load paths can revolutionise lightweight design across transport modes. Stiff and strong batteries that employ solid-state electrolytes and resilient electrodes and separators are generally lacking. Here we demonstrate a structural battery composite with unprecedented multifunctional performance (see Figure 12); featuring an energy density of 24 Wh kg^{-1} and an elastic modulus of 25 GPa and tensile strength exceeding 300 MPa. The first-generation structural battery is made from multifunctional constituents, where reinforcing carbon fibres act as electrode and current collector. A structural electrolyte is used for load transfer and ion transport and a glass fibre fabric separates the carbon fibre electrode from an aluminium foil supported lithium iron phosphate positive electrode. Equipped with these materials, lighter electrical cars, aircraft and consumer goods can be pursued.

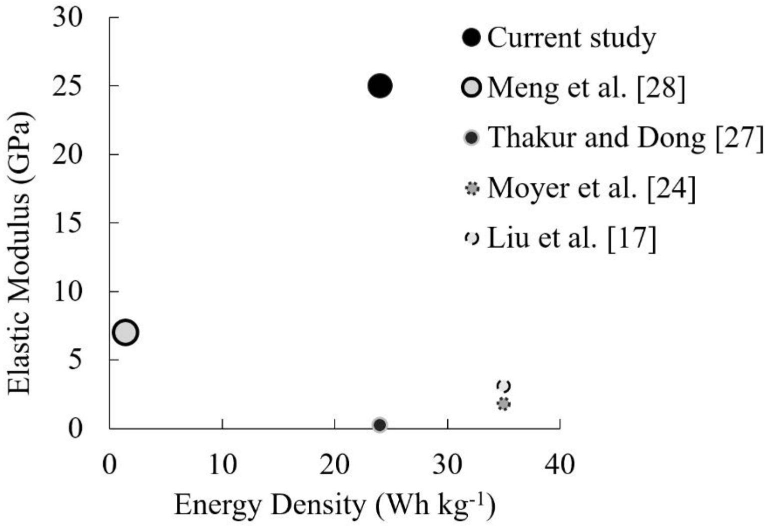

Figure 12: Elastic modulus and cell level energy density of the first-generation structural battery (labelled Current study) and data for structural battery composites presented in the literature.

Papers presented at international conferences with EOARD/AFOSR funding

Carlstedt D, Johannisson W, Zenkert D, Linde P, Asp LE. Conceptual design framework for laminated structural battery composites, 18th European Conference on Composite Materials, ECCM18, Athens, Greece, June 2018.

Asp LE, Carlstedt D, Duan S, Liu F. Characterisation of composite constituents for structural battery modelling, 11th Asian-Australasian Conference on Composite Materials, ACCM-11, Cairns, Australia, July, 2018.

Liu F, Duan S and Asp LE. Specimen preparation for transverse modulus measurement of carbon FIBREs using focused ion beam. Proc. ICCM22, Melbourne, Australia, 2019.

Duan S, Liu F, Pettersson T, Creighton C, Asp LE. Transverse modulus measurement of carbon fibre by Atomic force microscope and nanoindentation. Proc. ICCM22, Melbourne, Australia, 2019.

Carlstedt D, Xu J. Runesson K, Larsson F, Asp LE. Unit cells for Multiphysics modelling of structural battery composites. Proc. ICCM22, Melbourne, Australia, 2019.

Invited Keynote and Plenary presentations at international conferences

Asp LE, Composite materials for lightweight automotive applications. The 18th European Conference on Composite Materials, ECCM-18, Athens, Greece, June 2018 (**Keynote Lecture, audience approximately 1000**).

Asp LE, Main challenges in Composite Science in nearest 10 years, Advances in Composites Science and Technology, Bauman Moscow State Technical University, Moscow, December 2018 (**Plenary Lecture, audience approximately 1200**).

Asp LE. Characterisation and modelling of structural battery composites. ICCM22, Melbourne, Australia, 2019. (**Keynote Lecture, audience approximately 200**).

Multifunctional Materials

Electro-chemo-mechanically coupled computational modelling of structural batteries

To cite this article: David Carlstedt *et al* 2020 *Multifunct. Mater.* **3** 045002

IOP Publishing *Multifunct. Mater.* **3** (2020) 045002 https://doi.org/10.1088/2399-7532/abc60d

Multifunctional Materials

RECEIVED
1 September 2020

REVISED
6 October 2020

ACCEPTED FOR PUBLICATION
29 October 2020

PUBLISHED
19 November 2020

PAPER

Electro-chemo-mechanically coupled computational modelling of structural batteries

David Carlstedt, Kenneth Runesson, Fredrik Larsson, Johanna Xu and Leif E Asp

Department of Industrial and Materials Science, Chalmers University of Technology, SE-412 96 Gothenburg, Sweden

E-mail: leif.asp@chalmers.se

Keywords: Li-ion based structural batteries, multifunctional composites, electro-chemo-mechanical coupling, finite element analysis (FEA), multiphysics modelling

Abstract

Structural batteries are multifunctional composites that combine load-bearing capacity with electro-chemical energy storage capability. The laminated architecture is considered in this paper, whereby restriction is made to a so called half-cell in order to focus on the main characteristics and provide a computational tool for future parameter studies. A thermodynamically consistent modelling approach is exploited for the relevant electro-chemo-mechanical system. We consider effects of lithium insertion in the carbon fibres, leading to insertion strains, while assuming transverse isotropy. Further, stress-assisted ionic transport is accounted for in addition to standard diffusion and migration. The relevant space-variational problems that result from time discretisation are established and evaluated in some detail. The proposed model framework is applied to a generic/idealized material representation to demonstrate its functionality and the importance of accounting for the electro-chemo-mechanical coupling effects. As a proof of concept, the numerical studies reveal that it is vital to account for two-way coupling in order to predict the multifunctional (i.e. combined electro-chemo-mechanical) performance of structural batteries.

1. Introduction

In recent years, there has been a growing interest in multifunctional materials which can enable pathways for energy efficient and sustainable transportation [1–10]. One class of such materials is the structural battery, which has the ability to simultaneously carry mechanical load and store electro-chemical energy. By combining these functionalities, the structural battery offers significant mass and volume savings for future electric vehicles and devices [11–15].

Several possible microstructural design principles can be envisioned. The *laminated structural battery* architecture was first proposed by Wetzel *et al* [13] and later demonstrated by Ekstedt *et al* [16] and Carlson [17]. The individual laminae correspond to different components in a battery cell (electrodes, separator, etc). When these laminae are stacked into a laminate, the resulting material provides mechanical properties similar to those of conventional fibre reinforced polymer composites that are commonly used in structural applications (see e.g. work by Johannisson *et al* [18]).

The internal structure of a conventional lithium ion battery and the laminated structural battery are shown schematically in figure 1 for comparison. The negative and positive electrodes of the laminated structural battery consist of structural battery electrolyte (SBE) [19, 20] that is reinforced with carbon fibres. The SBE is a bi-continuous polymer network which contains liquid electrolyte. Hence, the SBE has the ability to both transfer mechanical load and transport ions. Since previous studies [21, 22] have shown good specific mechanical and electrical properties of carbon fibres, they are well suited for multifunctional applications. In the positive electrode the carbon fibres are coated with lithium metal oxide or olivine based particles, e.g. $LiFePO_4$, binder and conductive additives (see for example the work by Hagberg *et al* [23]). The two electrodes are separated by a porous polymer separator made from, e.g. a thin layer of SBE.

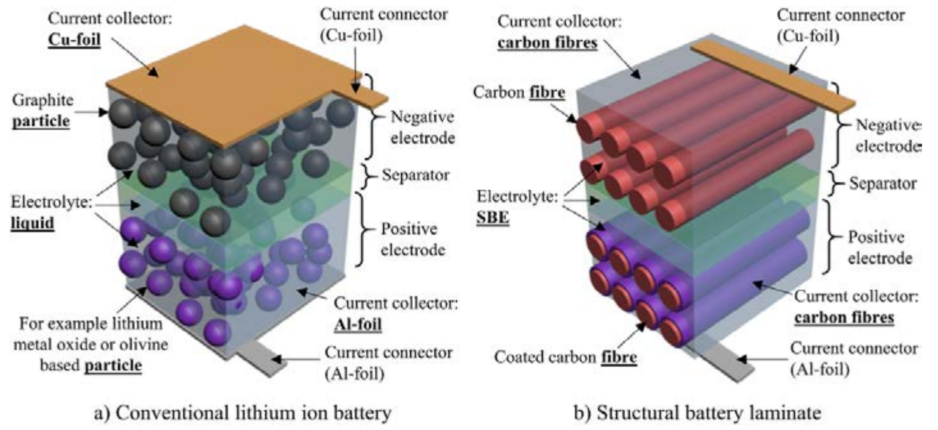

a) Conventional lithium ion battery

b) Structural battery laminate

Figure 1. Schematic illustration of (a) a conventional lithium ion battery and (b) the laminated structural battery. The bold underlined text represents the main differences between the two types of battery cells. SBE = Structural Battery Electrolyte.

The fibres in the negative electrode and the particles in the coating in the positive electrode act as active electrode materials (hosts for the lithium) in the structural battery cell.

In a conventional lithium ion battery, the electrodes consist of electrode particles and conductive additives (e.g. graphite particles and carbon black) adhered to a metal foil (current collector) using a polymer binder. The two electrodes are separated by a porous separator. This porous structure is soaked in a liquid electrolyte to allow for ion transport. Hence, the differences of the laminated structural battery cell, as compared to the conventional battery cell, are threefold: (i) The active electrode materials in the negative electrode are fibres instead of particles, (ii) SBE is used instead of liquid electrolyte and (iii) the fibres (in both electrodes) function as current collectors. The latter means that the upper and lower edges of the structural battery electrodes (see figure 1) do not need to be fully covered by metal foil like for the conventional battery cell. Furthermore, the ion conductivity of the SBE has been reported to be in the order of 10^{-4} S cm^{-1} [19, 20], whereas the conductivity of conventional liquid electrolytes is significantly higher, can be in the order of 10^{-2} S cm^{-1} [19, 24] at ambient temperature. Moreover, the electrical conductivity of carbon fibres [22] is about three orders of magnitude lower than for copper and aluminium, which are commonly used for current collectors in ordinary lithium ion batteries. This means that the geometric and topological characteristics of the cell, cf thickness of the different layers, volume fractions/fibre packaging, transportation properties of the constituents, etc are expected to have significant effects on the mechanical and electrical performance. There are currently no models available to assess these effects in structural batteries.

As to the theoretical prediction of the multifunctional properties and performance of the laminated structural battery, multiphysics modelling is needed. Apart from the seminal contributions by Newman and co-workers, e.g. [25–28], in the context of electro-chemo-mechanical modelling of conventional batteries with liquid and solid-state electrolytes, we note contributions by Purkayastha and McMeeking [29], Grazioli *et al* [30–32], Bucci *et al* [33], Wu and Lu [34], Ganser *et al* [35, 36], Xu *et al* [37], Wan and Ciucci [38], Bower *et al* [39] and Wu and Lu [40], to mention a few. Moreover, Salvadori *et al* [41–44] have developed multi-scale and computational homogenization approaches for modelling conventional Li-ion battery cells. Examples of review articles are Xu and Zhao [45] and Zhao *et al* [46]. Indeed, one may favourably apply the very same conceptual model framework to structural batteries while keeping in mind that the main differences are that carbon fibres are used as the active material in the negative electrode and as current collectors in both electrodes.

In previous work by the authors, [47–50], implications on the mechanical performance from electro-chemical cycling have been studied. These studies show that the distribution of the lithium inside the active electrode materials and heat generation due to electro-chemical cycling significantly affect the effective elastic properties of the composite and its internal stress state. In these studies, one-way coupling between the electro-chemical and mechanical response was assumed (i.e. the electro-chemical analysis was used to provide input for the mechanical analysis) to simplify the analyses, and simplified geometries (representative for the so-called 3D-battery architecture, see Leijonmarck *et al* [51]) were used. In the context of theoretical modelling of SBEs, Tu *et al* [52] have studied their bifunctional performance while assuming linear constitutive relations for stiffness and ionic conductivity. Moreover, Dionisi *et al* [53] and Johannisson *et al* [54] considered a strongly simplified geometry and a simplified electro-chemical process in order to adopt an analytical model for predicting deformations and stresses in laminated structural batteries and an electrochemical actuator, respectively, due to cyclic volume change of the active materials. In summary, a computational framework to study the fully coupled electro-chemo-mechanical response of the laminated structural battery is lacking.

In this paper, we take a further step towards solving the complete multiphysics problem for the laminated structural battery cell by adopting a thermodynamically consistent theoretical framework. In particular, this means that the constitutive relations for (the energetic parts of) mechanical stresses, electrochemical potentials and the electric flux density are derivable from a volume-specific free energy density for the bulk materials.[1] Most importantly, the relevant electric, chemical and mechanical fields are resolved for a realistic microstructural design and the appropriate interface and boundary conditions. Moreover, the highly anisotropic behaviour of the fibres in the longitudinal and radial directions (transverse isotropy) is modelled. Employing the general computational framework for analysis of the laminated structural battery architecture, our main objective is to demonstrate the importance of the two-way coupling between the electro-chemical and the mechanical response, on the one hand, and on the other hand, as a proof of concept.

The paper is organized as follows: In section 2 we present the conceptual microstructural features of the laminated structural battery cell. In section 3, we restrict the analysis to the simplified problem of the negative half-cell (to obtain a manageable problem). Further, we present the governing equations for the individual domains of interest (fibre, electrolyte) as well as for the fibre-electrolyte interface and the external boundaries including the positive and negative collectors. The complete formulation of the *potentiostatic* and *galvanostatic* problems are presented in section 4 in the context of the time-incremental weak format. In section 5 the numerical implementation in the commercial finite element (FE) software COMSOL Multiphysics® is described. Numerical results, as a proof of concept, are presented in section 6. Finally, concluding remarks and an outlook to future research are presented in section 7.

2. The conceptual microstructure of the laminated structural battery cell

2.1. Microstructural design

The considered typical microstructural design of a structural battery composite, more specifically a so called laminated battery design, is shown in figure 2. The idea of the laminated design is to stack the laminae in such a fashion that the resulting mechanical properties become similar to those of conventional fibre reinforced polymer composites as well as providing an efficient battery function. The laminated micro-battery components are identified as follows:

- The negative electrode (upper lamina in figure 2(a)): carbon fibres, with the ability to (de)insert (neutral) Li-ions, are embedded in a porous matrix (SBE). The typical radius of the fibres is 2.5 μm and the distance between the centre position of the fibres depends on the volume fraction of fibres. For a fibre volume fraction of 0.3 (assuming square fibre packing arrangement) this distance is 8.1 μm.
- The positive electrode (lower lamina in figure 2(a)): carbon fibres, coated with a mixture containing Li-metal-oxide or olivine based particles (such as $LiFePO_4$) and conductive additives (such as carbon black), are embedded in SBE. The typical thickness of the coating varies from around 1 μm to several micrometres (Hagberg *et al* [23]).
- Separator/SBE (middle lamina in figure 2(a)): The separator is assumed to be made from SBE. The existence of a separator lamina assures that the active electrode materials in the two electrodes do not come in contact.

When the battery is charged, the current is brought about by Li-ions that are transported (migrate and diffuse) from the positive electrode (coating) through the separator and enters the negative electrode (fibre). Inside the fibres it is assumed that the Li-ion is neutralized and the current is conducted by electronic activity (whereby the current flows in the opposite direction to that of the electrons). When the battery is discharged the flow direction of ions and electrons is reversed.

2.2. Simplified architecture: The negative half-cell

It is possible to simplify the theoretical analysis and experimental investigation of the laminated structural battery cell by using the similarity of the two electrodes in the laminated architecture (both the negative and positive electrodes consist of fibres embedded in a SBE-based matrix material, as discussed above). It should however be noted that the main difference between the electrodes is that in the negative electrode the fibres act as the host for the lithium (i.e. expand/shrink) and current collectors simultaneously. In contrast, in the positive electrode the particles in the coating act as host for the lithium and the fibres only function as current collectors. Hence, in the negative electrode the carbon fibres will expand/shrink due to lithium

---

[1] The explicit expressions of the various contributions to the free energy are not elaborated in this paper.

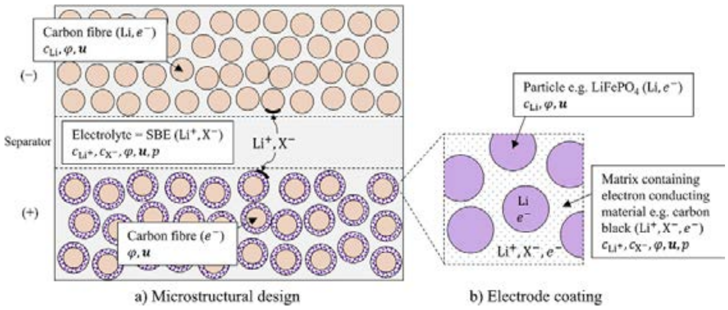

a) Microstructural design   b) Electrode coating

Figure 2. (a) Possible (micro)structural design of the structural battery composite comprising (−) and (+) electrodes with carbon fibres embedded in porous polymer electrolyte matrix (SBE). (b) Electrode coating with embedded Li-rich particles and matrix containing electron conductor (carbon black). The introduced notation is defined in section 3.

insertion/extraction while in the positive electrode the particles in the coating will undergo such volume changes. Moreover, properties of the coating (e.g. particle size, distribution, etc) need to be incorporated in the model. Depending on the particle size (in comparison with dimensions of the fibres), the particles may need to be modelled explicitly or homogenized properties of the coating domain may be utilized. The provided framework can be used for modelling both electrodes but due to the relative maturity and the availability of experimental data, the negative electrode is selected for this study. We shall thus consider the negative half-cell in figure 3, which corresponds to the battery cell that was experimentally studied in previous works [18–20]. In principle, the positive electrode in the full-cell has been replaced by merely the collector of solid Li-metal. Moreover, the separator is excluded in the model (for simplicity).

3. Time-continuous strong format: Individual domains, interfaces and boundaries

In this section the time-continuous strong format and modelling assumptions for the individual domains, interfaces and boundaries are presented. A general model assumption is isothermal condition, i.e. the absolute temperature $\theta(\boldsymbol{x}, t) = \theta_0(\boldsymbol{x})$ is only a given parameter. As to the mechanical properties, it is assumed that all material phases are linear elastic (small deformations). However, material nonlinearities are present in the electro-chemical relations. Self-weight is ignored, i.e. no body load is present. Finally, any piezoelectric effect is ignored, which means (in particular) that stresses do not depend explicitly on the electric field.

3.1. Fibre domain(s) $\Omega_{\mathbf{f}} = \cup_i^{N_{\mathbf{fibres}}} \Omega_{\mathbf{f},i}$

The following special assumptions are introduced: (i) The material properties are characterized as transversely isotropic, whereby isotropy pertains to the cross-section (Cartesian coordinates x_1, x_2); (ii) The single active species is Li, which is neutral and can move into the carbon fibre material; (iii) In the external connection (connecting Ω_{f} to Γ_+) all current is carried by electron transport. However, all fibres (which serve as the negative electrode) are connected to a collector with the *same* potential $\Phi^-(t)$. Due to the high electronic conductivity (as compared to the ionic conductivity), the potential is assumed uniform, $\varphi(\boldsymbol{x}, t) = \Phi^-(t)$, for $\boldsymbol{x} \in \Omega_{\mathrm{f}} = \cup_i^{N_{\mathrm{fibres}}} \Omega_{\mathrm{f},i}$. As a consequence, the electric field vanishes and the current is not resolved in the fibres (figure 3(d)). We remark that the value $\Phi^-(t)$ is either given *a priori* (potentiostatic problem) or is computed as part of the problem solution (galvanostatic problem).

We summarize the governing balance equations in the strong format:

$$-\boldsymbol{\sigma} \cdot \boldsymbol{\nabla} = \boldsymbol{0} \text{ in } \Omega_{\mathrm{f}} \times \mathbb{R}^+ \tag{1a}$$

$$-\partial_t c_{\mathrm{Li}} - \boldsymbol{j}_{\mathrm{Li}} \cdot \boldsymbol{\nabla} = 0 \text{ in } \Omega_{\mathrm{f}} \times \mathbb{R}^+ \tag{1b}$$

where $\boldsymbol{\sigma}$ is the (symmetric) stress tensor, $\boldsymbol{j}_{\mathrm{Li}}$ is the mass flux vector for lithium and c_{Li} is the mass concentration (molarity) of lithium.

The relevant constitutive relations are:

$$\boldsymbol{\sigma} = \mathsf{E} : \left[\boldsymbol{\epsilon}[\boldsymbol{u}] - \boldsymbol{\epsilon}^{\mathrm{ch}}(c_{\mathrm{Li}})\right] \tag{2a}$$

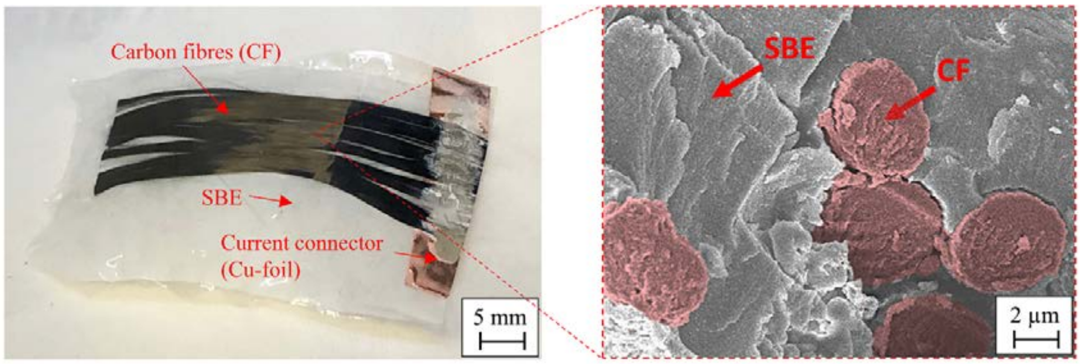

a) Negative electrode lamina

b) Cross-section (SEM image)

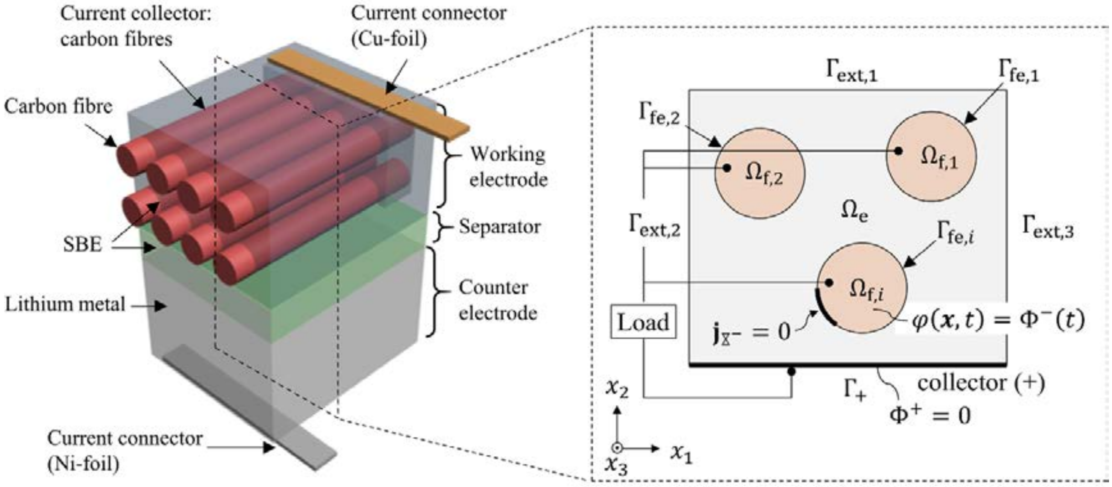

c) Schematic architecture: negative half-cell

d) Model representation

Figure 3. (a) Photo of a negative electrode lamina (carbon fibres in SBE). (b) SEM-image of the cross section of the negative electrode (CF = carbon fibre). (c) Schematic architecture of the negative half-cell that was experimentally studied in previous works [18–20]. (d) Illustration of the considered idealized half-cell. In the external circuit, Load represents electric Loading, e.g. in terms of a given resistance. The introduced notation is defined in section 3.

$$\boldsymbol{j}_{\mathrm{Li}} = -\boldsymbol{M}_{\mathrm{Li}} \cdot \boldsymbol{\nabla} \mu_{\mathrm{Li}} \tag{2b}$$

$$\text{where } \mu_{\mathrm{Li}} = -\zeta \boldsymbol{\alpha}^{\mathrm{ch}} : \boldsymbol{\sigma}(\boldsymbol{\epsilon}, c_{\mathrm{Li}}) + \mu^{0}_{\mathrm{Li}} + R\theta_0 \log\left(f_{\mathrm{Li}}(\tilde{c}_{\mathrm{Li}})\tilde{c}_{\mathrm{Li}}\right) \tag{2c}$$

where $\boldsymbol{\epsilon}[\boldsymbol{u}]$ is the (small) strain tensor expressed as a linear operator of the displacement field $\boldsymbol{u}$, and μ_{Li} is the chemical potential for Li. Moreover, $\tilde{c}_{\mathrm{Li}}$ is the normalized mass concentration of Li w.r.t. its maximum concentration, $c_{\mathrm{Li,max}}$, thus defined as $\tilde{c}_{\mathrm{Li}} = \frac{c_{\mathrm{Li}}}{c_{\mathrm{Li,max}}}$.

As to the material properties, we introduced the elasticity tensor that is pertinent to transverse isotropy as follows:

$$\begin{aligned}\mathsf{E} = \quad & L_\perp \boldsymbol{I} \otimes \boldsymbol{I} + 2G_\perp \mathsf{I}^{\mathrm{sym}} + [L_\| - L_\perp][\boldsymbol{I} \otimes \boldsymbol{E}_3 + \boldsymbol{E}_3 \otimes \boldsymbol{I}] \\ & + [2G_\perp - 2G_\| - L_\| + L_\perp]\boldsymbol{E}_3 \otimes \boldsymbol{E}_3 + 4[G_\| - G_\perp]\mathsf{A}\end{aligned} \tag{3}$$

where $\boldsymbol{I} = \boldsymbol{E}_1 + \boldsymbol{E}_2 + \boldsymbol{E}_3$ is the 2nd order identity tensor ($\boldsymbol{E}_i := \boldsymbol{e}_i \otimes \boldsymbol{e}_i$ is the ith base dyad), $\mathsf{I}^{\mathrm{sym}} := \frac{1}{2}[\boldsymbol{I} \overline{\otimes} \boldsymbol{I} + \boldsymbol{I} \underline{\otimes} \boldsymbol{I}]$ is the (symmetric) 4th order identity tensor,[2] whereas $\mathsf{A} := \frac{1}{4}[\boldsymbol{E}_3 \overline{\otimes} \boldsymbol{I} + \boldsymbol{E}_3 \underline{\otimes} \boldsymbol{I} + \boldsymbol{I} \overline{\otimes} \boldsymbol{E}_3 + \boldsymbol{I} \underline{\otimes} \boldsymbol{E}_3]$ is a 4th order symmetric tensor. Lamé's first parameter is denoted L and the shear modulus[3] is denoted G.

---

[2] Indicial notation: $(\boldsymbol{A} \overline{\otimes} \boldsymbol{B})_{ijkl} \overset{\mathrm{def}}{=} (\boldsymbol{A})_{ik}(\boldsymbol{B})_{jl}$, $(\boldsymbol{A} \underline{\otimes} \boldsymbol{B})_{ijkl} \overset{\mathrm{def}}{=} (\boldsymbol{A})_{il}(\boldsymbol{B})_{jk}$ for $\boldsymbol{A}, \boldsymbol{B}$ symmetric 2nd order tensors.

[3] The explicit representation of E in Voigt matrix notation is presented in appendix A, for clarity.

Further, we introduced the lithium insertion strain $\boldsymbol{\epsilon}^{\mathrm{ch}}(c_{\mathrm{Li}})$ and the mobility tensor $\boldsymbol{M}_{\mathrm{Li}}(c_{\mathrm{Li}})$ as follows:

$$\boldsymbol{\epsilon}^{\mathrm{ch}}(c_{\mathrm{Li}}) = \zeta \boldsymbol{\alpha}^{\mathrm{ch}} \left[c_{\mathrm{Li}} - c_{\mathrm{Li,ref}}\right], \quad \text{with } \boldsymbol{\alpha}^{\mathrm{ch}} = \alpha_{\perp}^{\mathrm{ch}} \left[\boldsymbol{E}_1 + \boldsymbol{E}_2\right] + \alpha_{||}^{\mathrm{ch}} \boldsymbol{E}_3 \tag{4a}$$

$$\boldsymbol{M}_{\mathrm{Li}}(c_{\mathrm{Li}}) = M_{\mathrm{Li},\perp}(c_{\mathrm{Li}}) \left[\boldsymbol{E}_1 + \boldsymbol{E}_2\right] + M_{\mathrm{Li},||}(c_{\mathrm{Li}}) \boldsymbol{E}_3 \tag{4b}$$

where the coefficient $\zeta = c_{\mathrm{Li,max}}^{-1}$ is introduced for dimensionality and $\boldsymbol{\alpha}^{\mathrm{ch}}$ is a second order tensor containing the transversely isotropic coefficients of the insertion induced expansion/shrinkage of the fibres. Moreover, the reference value $c_{\mathrm{Li,ref}}$ defines the state at which no chemical strains are present in the material. For simplicity, it is set equal to 0. Furthermore, the mobilities in the fibres in the transverse and longitudinal directions are assumed equal and are defined as: $M_{\mathrm{Li},\perp}(c_{\mathrm{Li}}) = M_{\mathrm{Li},||}(c_{\mathrm{Li}}) = \eta_{\mathrm{Li}} c_{\mathrm{Li}}$, where η_{Li} is the mobility coefficient of Li in the fibres.

The constitutive relation for the chemical potential μ_{Li} consists of two parts: The first part $\zeta \boldsymbol{\alpha}^{\mathrm{ch}} : \boldsymbol{\sigma}(\boldsymbol{\epsilon}, c_{\mathrm{Li}})$ represents the stress-driven diffusion. The second part represents standard concentration-driven diffusion. As to the model parameters, μ_{Li}^{0} is a reference/standard value for the pure species, R is the universal gas constant and θ_0 is a reference temperature. The activity coefficient f_{Li} is chosen in accordance with the definition for an ideal solid solution of non-interacting particles on a lattice in Bazant [55]: $f_{\mathrm{Li}}(\tilde{c}_{\mathrm{Li}}) = \frac{1}{1-\tilde{c}_{\mathrm{Li}}}$.
Remark 1. *Due to the transverese isotropy of fibres, the contribution from stress to* μ_{Li} *involves not only the mean stress; indeed, it is only in the case of isotropy [when* $\boldsymbol{\alpha}^{\mathrm{ch}} = \alpha^{\mathrm{ch}} \boldsymbol{I}$*] that* $\boldsymbol{\alpha}^{\mathrm{ch}} : \boldsymbol{\sigma} = 3\alpha^{\mathrm{ch}} \sigma_{\mathrm{m}}$*, where* $\sigma_{\mathrm{m}} := \frac{1}{3}[\sigma_{11} + \sigma_{22} + \sigma_{33}]$*, see Xu et al [37].*

3.2. Electrolyte domain Ω_{e}

The following special assumptions are introduced: (i) The material properties are characterized as isotropic; (ii) The Li-ions are positively charged (cation, Li^{+}), whereas the companion X-ions (anion, e.g. PF_6^{-}) are negatively charged. Insertion does not occur in the electrolyte; (iii) The current density is carried both by Li^{+} and the companion X^{-}. No electronic activity is permitted, i.e. no current due to motion of electrons $\boldsymbol{i}_{\mathrm{e}^-} = \boldsymbol{0}$; (iv) The electric potential φ may be discontinuous along each fibre-matrix interface $\Gamma_{\mathrm{fe},i},\ i = 1, 2, \ldots, N_{\mathrm{fibres}}$. This discontinuity is modelled via a linearized Butler–Volmer type of 'electric resistance' relation. This relation, which involves the potential φ in the electrolyte (along the interface) and the value Φ^{-} in the fibres, will serve as a Robin type boundary condition along each $\Gamma_{\mathrm{fe},i}$ (see below).

We summarize the governing balance equations in the strong format:

$$-\boldsymbol{\sigma} \cdot \boldsymbol{\nabla} = \boldsymbol{0} \text{ in } \Omega_{\mathrm{e}} \times \mathbb{R}^{+} \tag{5a}$$

$$-\boldsymbol{i}_{\mathrm{MAX}} \cdot \boldsymbol{\nabla} = 0 \text{ in } \Omega_{\mathrm{e}} \times \mathbb{R}^{+} \tag{5b}$$

$$-\partial_t c_{\mathrm{Li}} - \boldsymbol{j}_{\mathrm{Li}} \cdot \boldsymbol{\nabla} = 0 \text{ in } \Omega_{\mathrm{e}} \times \mathbb{R}^{+} \tag{5c}$$

$$-\partial_t c_{\mathrm{X}} - \boldsymbol{j}_{\mathrm{X}} \cdot \boldsymbol{\nabla} = 0 \text{ in } \Omega_{\mathrm{e}} \times \mathbb{R}^{+} \tag{5d}$$

where $\boldsymbol{i}_{\mathrm{MAX}} := \partial_t \boldsymbol{d} + \boldsymbol{i}_{\mathrm{ions}}$ is the Maxwell current density that is composed of two contributions: $\boldsymbol{d}$ is the electric flux density vector (dielectric displacement), whereas $\boldsymbol{i}_{\mathrm{ions}} = z'_{\mathrm{Li}} \boldsymbol{j}_{\mathrm{Li}} + z'_{\mathrm{X}} \boldsymbol{j}_{\mathrm{X}}$ is the current density due to motion of ions (known as Faraday's law of electrolysis). Here we introduced the specific charge $z'_{\alpha} = F z_{\alpha}$ for $\alpha = \mathrm{Li,X}$, where z_{α} is the valence number and F is Faraday's constant. Moreover, we define the normalized mass concentration of species Li and X in the electrolyte as $\tilde{c}_{\mathrm{Li}} = \frac{c_{\mathrm{Li}}}{c_{\mathrm{Li,ref}}}$ and $\tilde{c}_{\mathrm{X}} = \frac{c_{\mathrm{X}}}{c_{\mathrm{X,ref}}}$, respectively. Both $c_{\mathrm{Li,ref}}$ and $c_{\mathrm{X,ref}}$ are set to 1 molar (or 1000 $\mathrm{mol\,m^{-3}}$). Further, $\boldsymbol{j}_{\mathrm{X}}$ is the mass flux vector for species X.

The relevant constitutive relations are:

$$\boldsymbol{\sigma} = \mathsf{E} : \boldsymbol{\epsilon}[\boldsymbol{u}] \tag{6a}$$

$$\boldsymbol{d} = -\boldsymbol{\mathcal{E}} \cdot \boldsymbol{\nabla} \varphi \tag{6b}$$

$$\boldsymbol{j}_{\mathrm{Li}} = -\boldsymbol{M}_{\mathrm{Li}} \cdot \boldsymbol{\nabla}\mu_{\mathrm{Li}} - \boldsymbol{\mathcal{L}}_{\mathrm{Li}} \cdot \boldsymbol{\nabla}\varphi \tag{6c}$$

$$\text{where } \mu_{\mathrm{Li}} = \mu^0_{\mathrm{Li}} + R\theta_0 \log\left(f_{\mathrm{Li}}(\tilde{c}_{\mathrm{Li}})\tilde{c}_{\mathrm{Li}}\right) \tag{6d}$$

$$\boldsymbol{j}_{\mathrm{X}} = -\boldsymbol{M}_{\mathrm{X}} \cdot \boldsymbol{\nabla}\mu_{\mathrm{X}} - \boldsymbol{\mathcal{L}}_{\mathrm{X}} \cdot \boldsymbol{\nabla}\varphi \tag{6e}$$

$$\text{where } \mu_{\mathrm{X}} = \mu^0_{\mathrm{X}} + R\theta_0 \log\left(f_{\mathrm{X}}(\tilde{c}_{\mathrm{X}})\tilde{c}_{\mathrm{X}}\right) \tag{6f}$$

where we introduced the notation $\boldsymbol{\mathcal{L}}_\alpha := z'_\alpha \boldsymbol{M}_\alpha$ for $\alpha = \mathrm{Li,X}$.

We introduced the standard isotropic elasticity tensor

$$\mathsf{E} = L\boldsymbol{I} \otimes \boldsymbol{I} + 2G\mathsf{I}^{\mathrm{sym}} \tag{7}$$

and Lame's parameters can be expressed in terms of Young's modulus (E) and Poisson's ratio (ν) as follows: $L = \frac{E\nu}{[1+\nu][1-2\nu]}$ and $G = \frac{E}{2[1+\nu]}$.

We also introduced the isotropic permittivity tensor $\boldsymbol{\mathcal{E}} := \varepsilon \boldsymbol{I}$, where $\varepsilon = \varepsilon_0\varepsilon_r$ is the permittivity (i.e. the material's ability to transmit an electric field). The permittivity in vacuum is denoted ε_0 and the relative permittivity is denoted ε_r. Moreover, φ is the electrical potential and μ_{X} is the chemical potential for species X. The activity coefficients are assumed constant and equal to 1 in the electrolyte ($f_{\mathrm{Li}}(\tilde{c}_{\mathrm{Li}}) = f_{\mathrm{X}}(\tilde{c}_{\mathrm{X}}) = 1$). Moreover, the isotropic mobility tensors $\boldsymbol{M}_{\mathrm{Li}}(c_{\mathrm{Li}})$, $\boldsymbol{M}_{\mathrm{X}}(c_{\mathrm{X}})$, are defined as follows:

$$\boldsymbol{M}_{\mathrm{Li}}(c_{\mathrm{Li}}) = M_{\mathrm{Li}}(c_{\mathrm{Li}})\boldsymbol{I} \tag{8a}$$

$$\boldsymbol{M}_{\mathrm{X}}(c_{\mathrm{X}}) = M_{\mathrm{X}}(c_{\mathrm{X}})\boldsymbol{I} \tag{8b}$$

Here, we made the simplification that there is no coupling between the diffusion of Li^+ and X^-. Moreover, the mobilities are defined as: $M_{\mathrm{Li}}(c_{\mathrm{Li}}) = \eta_{\mathrm{Li}} c_{\mathrm{Li}}$ and $M_{\mathrm{X}}(c_{\mathrm{X}}) = \eta_{\mathrm{X}} c_{\mathrm{X}}$, where η_α is the mobility coefficient of species α for $\alpha = \mathrm{Li, X}$ in the electrolyte.

Finally, combining the expressions above, we derive the constitutive relation for the Maxwell current:

$$\boldsymbol{i}_{\mathrm{MAX}} = -\boldsymbol{\mathcal{L}}_{\mathrm{Li}} \cdot \boldsymbol{\nabla}\mu_{\mathrm{Li}} - \boldsymbol{\mathcal{L}}_{\mathrm{X}} \cdot \boldsymbol{\nabla}\mu_{\mathrm{X}} - \boldsymbol{\mathcal{K}}^{\mathrm{eff}} \cdot \boldsymbol{\nabla}\varphi - \boldsymbol{\mathcal{E}} \cdot \partial_t \boldsymbol{\nabla}\varphi \tag{9}$$

where we introduced the 'effective' electric conductivity $\boldsymbol{\mathcal{K}}^{\mathrm{eff}} \overset{\mathrm{def}}{=} [z'_{\mathrm{Li}}]^2 \boldsymbol{M}_{\mathrm{Li}} + [z'_{\mathrm{X}}]^2 \boldsymbol{M}_{\mathrm{X}}$.

3.3. The fibre/electrolyte interface Γ_{fe}

It is assumed that the redox reactions and load transfer occur along the entire fibre/electrolyte interface while assuming uniform properties. As to the mechanical integrity, it is assumed that the interface is perfectly bonded such that the displacement field $\boldsymbol{u}$ as well as the traction ($\boldsymbol{\sigma}_n = \boldsymbol{\sigma} \cdot \boldsymbol{n}$, where $\boldsymbol{n}$ is the normal on Γ_{fe} pointing out from the fibre domain Ω_{f}) are continuous across Γ_{fe}.

Next, we consider the electrochemical conditions. Firstly, due to redox reactions, the electrically charged Li-ion will pick up an electron and become neutral when passing through Γ_{fe} from Ω_{e} to Ω_{f}, whereafter it becomes inserted in the carbon fibre. Next, we assume that μ_{Li}, as well as φ, may be discontinuous across Γ_{fe}, whereas $j_{\mathrm{Li},n}$ is continuous across Γ_{fe}. A simple, yet very useful (as will be shown below), assumption is that $j_{\mathrm{Li},n}$ is governed constitutively by an interface mobility $\bar{M}$ such that

$$j_{\mathrm{Li},n}(\boldsymbol{x}) := \boldsymbol{j}_{\mathrm{Li}}(\boldsymbol{x}) \cdot \boldsymbol{n}(\boldsymbol{x}) = -\bar{M}[[\mu'_{\mathrm{Li}}]](\boldsymbol{x}) = -\bar{M}[[\mu_{\mathrm{Li}}]](\boldsymbol{x}) - \bar{\mathcal{L}}\left[\varphi^{\mathrm{e}} - \Phi^-\right],\ \boldsymbol{x} \in \Gamma_{\mathrm{fe}} \tag{10}$$

where we define $\bar{\mathcal{L}} := z'_{\mathrm{Li}}\bar{M}$. Here, we introduced the jump operator $[[\bullet]](\boldsymbol{x}) := \bullet(\boldsymbol{x}^{\mathrm{e}}) - \bullet(\boldsymbol{x}^{\mathrm{f}})$ and $\boldsymbol{x}^{\mathrm{e}} := \lim_{\epsilon\downarrow 0} \boldsymbol{x} + \epsilon\boldsymbol{n}$, $\boldsymbol{x}^{\mathrm{f}} := \lim_{\epsilon\downarrow 0} \boldsymbol{x} - \epsilon\boldsymbol{n}$. Moreover, we used the identity $[[\mu'_{\mathrm{Li}}]] = [[\mu_{\mathrm{Li}}]] + z'_{\mathrm{Li}}[\varphi^{\mathrm{e}} - \Phi^-]$, where z'_{Li} is assumed continuous across Γ_{fe} and where $\varphi^{\mathrm{e}} := \varphi(\boldsymbol{x}^{\mathrm{e}})$ is the electric potential in the electrolyte at the fibre-electrolyte interface. Clearly, this model carries over directly to the current density flux i_n and, consequently, to $i_{\mathrm{MAX},n}$ across the interface Γ_{fe}. To this end, we first obtain

$$i_n = z'_{\mathrm{Li}} j_{\mathrm{Li},n} + z'_{\mathrm{X}} \underbrace{j_{\mathrm{X},n}}_{=0} = -\bar{\mathcal{L}}[[\mu_{\mathrm{Li}}]] - \bar{\mathcal{K}}^{\mathrm{eff}}\left[\varphi^{\mathrm{e}} - \Phi^-\right] \text{ on } \Gamma_{\mathrm{fe}} \tag{11}$$

where we introduced the assumption $j_{\mathrm{X},n}(\boldsymbol{x}^{\mathrm{e}}) = 0,\ \boldsymbol{x} \in \Gamma_{\mathrm{fe}}$, i.e. the transport of X^- is blocked at the fibre-electrolyte interface. Further, we introduced the 'effective conductivity' $\bar{\mathcal{K}}^{\mathrm{eff}} := [z'_{\mathrm{Li}}]^2 \bar{M} = z'_{\mathrm{Li}} \bar{\mathcal{L}}$. Next, we introduce the constitutive assumption

$$d_n = -\bar{\mathcal{E}}\left[\varphi^{\mathrm{e}} - \Phi^-\right] \text{ on } \Gamma_{\mathrm{fe}} \tag{12}$$

Now, noting that $i_{\mathrm{Max},n} = \partial_t d_n + i_n$, we are in the position to give the constitutive relation for $i_{\mathrm{Max},n}$ as follows:

$$i_{\mathrm{Max},n} = -\bar{\mathcal{L}}[[\mu_{\mathrm{Li}}]] - \left[\bar{\mathcal{K}}^{\mathrm{eff}} + \bar{\mathcal{E}}\partial_t\right]\left[\varphi^{\mathrm{e}} - \Phi^-\right] \text{ on } \Gamma_{\mathrm{fe}} \tag{13}$$

Remark 2. *It is of considerable interest to look into the nature of the relation for* i_n *in equation (11). Recalling the explicit expressions for the chemical potential* μ_{Li}*, as defined in equation (2c), we may rewrite* $[[\mu_{\mathrm{Li}}]]$ *as follows:*

$$[[\mu_{\mathrm{Li}}]] = \zeta \boldsymbol{\alpha}^{\mathrm{ch}} : \boldsymbol{\sigma} + z'_{\mathrm{Li}} U_{\mathrm{eq}}(\tilde{c}^{\mathrm{e}}_{\mathrm{Li}}, \tilde{c}^{\mathrm{f}}_{\mathrm{Li}}) \tag{14}$$

where $\tilde{c}^{\mathrm{e}}_{\mathrm{Li}}$ *and* $\tilde{c}^{\mathrm{f}}_{\mathrm{Li}}$ *are the normalized Li-concentration in the electrolyte and fibre, respectively, and* U_{eq} *is the so called equilibrium potential*

$$U_{\mathrm{eq}}(\tilde{c}^{\mathrm{e}}_{\mathrm{Li}}, \tilde{c}^{\mathrm{f}}_{\mathrm{Li}}) = \frac{1}{z'_{\mathrm{Li}}}\left[\mu^{0,\mathrm{e}}_{\mathrm{Li}} - \mu^{0,\mathrm{f}}_{\mathrm{Li}} - R\theta_0 \log\left(\frac{\tilde{c}^{\mathrm{f}}_{\mathrm{Li}}}{1 - \tilde{c}^{\mathrm{f}}_{\mathrm{Li}}} \frac{1}{\tilde{c}^{\mathrm{e}}_{\mathrm{Li}}}\right)\right] \tag{15}$$

that is completely consistent with the choice of the chemical potential μ *in the fibre and the electrolyte in equations (2c) and (6d), respectively. This corresponds to the Nernst equation, see Newman and Thomas-Alyea [28]. To capture the features of the equilibrium potential of the carbon fibres in a more realistic fashion, it is possible to refine the chosen simple format of the activity coefficient* $f^{\mathrm{f}}_{\mathrm{Li}}$ *(e.g. as done in Doyle et al [26]). Hence, equation (11) can be written more explicitly as*

$$i_n = -\bar{\mathcal{L}}[\zeta \boldsymbol{\alpha}^{\mathrm{ch}} : \boldsymbol{\sigma}] - \bar{\mathcal{K}}^{\mathrm{eff}}\left[\varphi^{\mathrm{e}} - \Phi^- + U_{\mathrm{eq}}\right] \text{ on } \Gamma_{\mathrm{fe}} \tag{16}$$

When stress-driven diffusion is ignored (which is the classical situation in the electro-chemistry literature), it is possible to identify the expression in equation (16) as a linearization of the classical Butler–Volmer expression, which reads

$$i_n = i_0\left[\exp\left(\frac{\bar{S}\bar{\eta}}{2}\right) - \exp\left(-\frac{\bar{S}\bar{\eta}}{2}\right)\right] \tag{17}$$

where $\bar{\eta}$ *is defined as* $\bar{\eta}(\boldsymbol{x}) := -\left[\varphi^{\mathrm{e}} - \Phi^- + U_{\mathrm{eq}}\right],\ \boldsymbol{x} \in \Gamma_{\mathrm{fe}}$*, and is the so called 'surface overpotential'. Further,* $\bar{S}$ *is the resistance coefficient,* $\bar{S} = \frac{F}{R\theta_0}$*. For small values of* $\bar{\eta}$ *it is possible to linearize this expression, whereby equation (16) (without the stress-diffusion term) is obtained with the identity* $\bar{\mathcal{K}}^{\mathrm{eff}} = i_0 \bar{S}$*.*

The current $I^-(t)$ corresponds to the total current in all the fibres that are connected to the negative connector (e.g. a strip of metal foil) that is assumed to be attached at the fibre ends. Clearly, this current has to be transported/conducted via electronic conduction along the fibres; however, it cannot be modelled in a 2D-setting. Its value is known (prescribed) in the case of a galvanostatic problem, whereas it is a 'reaction' in the case of a potentiostatic problem, when Φ^- is prescribed. In the latter case the corresponding test function is set to zero.

In either case we have the condition

$$\int_{\Gamma_{\mathrm{fe}}} i_{\mathrm{MAX},n} \mathrm{d}S = I^-_{\mathrm{MAX}} \tag{18}$$

which can be rephrased in the weak form as part of the galvanostatic problem.

3.4. Exterior boundaries $\Gamma_{\mathrm{ext}} \cup \Gamma_+$

Conditions at the exterior boundaries are imposed (typically) as follows:

Mechanical conditions:

$$u_1 = 0,\ \sigma_{n,2} = 0 \text{ on } \Gamma_{\mathrm{ext},2} \cup \Gamma_{\mathrm{ext},3} \tag{19a}$$

$$\boldsymbol{\sigma}_n = \boldsymbol{0} \text{ on } \Gamma_{\mathrm{ext},1} \cup \Gamma_+ \tag{19b}$$

The motivation for the traction-free condition on $\Gamma_{\text{ext},1} \cup \Gamma_{+}$ in equation (19*b*) is that the studied (part of the) lamina will in practice constitute a layered plate structure, whereby the assumption about small magnitude of the normal stress across the plate thickness is well taken.

Chemical conditions:

$$j_{\text{Li},n} = -\bar{\mathcal{L}}\left[\Phi^{+} - \varphi^{\text{e}}\right] \ \text{ on } \Gamma_{+} \tag{20a}$$

$$j_{\text{Li},n} = 0 \ \text{ on } \Gamma_{\text{ext}} \tag{20b}$$

$$j_{\text{X},n} = 0 \ \text{ on } \Gamma_{\text{ext}} \cup \Gamma_{+} \tag{20c}$$

The assumed chemical conditions are motivated by the fact that the mass flux occurs between the Li-metal and fibres (i.e. mainly in the x_2-direction in figure 3(d)) and that the height of the studied unit corresponds to the thickness of the electrode lamina.

Electrical conditions:

$$i_{\text{Max},n} = -\left[\bar{\mathcal{K}}^{\text{eff}} + \bar{\mathcal{E}}\partial_t\right]\left[\Phi^{+} - \varphi^{\text{e}}\right] \ \text{ on } \Gamma_{+} \tag{21a}$$

$$i_{\text{Max},n} = 0 \ \text{ on } \Gamma_{\text{ext}} \tag{21b}$$

where it is noted that Φ^{+} is a spatially constant value in the collector (Li-metal) just outside Γ_{+} and φ^{e} is the electrolyte potential along Γ_{+}. Moreover, we assume that Φ^{+} is henceforth prescribed at 0 V (as a given reference potential).

3.5. System characteristics for discharging and (re)charging phases

The basic problem formulations are the potentiostatic and galvanostatic problems, whereby the potential $\Phi^{-}(t)$ and the current $I^{-}(t)$, respectively, is the controlled (prescribed) quantity. A more general situation is that the battery cell is connected to an external circuit that contains an 'electric loading device', see figure 3(d). In such a situation neither $\Phi^{-}(t)$, nor $I^{-}(t)$, is known; rather, they are both part of the problem solution.

Here we use the convention of a carbon fibre electrode vs. Li-metal half-cell, i.e. lithiation of the fibres is referred to as discharge and delithiation as charge. We are now in position to characterize the distinct phases of discharging and charging (which can be repeated in a cyclic fashion):

Charging (delithiation): During the charging phase, the electric loading device is disconnected and either a potentiostatic or galvanostatic problem is solved. This phase ends when the battery is fully charged, which is the case when either $\Phi^{-}(t)$ or $I^{-}(t)$ reaches a predefined threshold value. Given the selected convention, charging corresponds to delithiation of the fibres.

Discharging (lithiation): During the discharging phase, the electric loading device is connected. This phase ends when either $\Phi^{-}(t)$ or $I^{-}(t)$ falls below a predefined threshold value. Given the selected convention, discharging corresponds to lithiation of the fibres.

4. Time-incremental weak format of half-cell problem

4.1. Preliminaries

Let us introduce time intervals $I_n = (t_{n-1}, t_n)$, whose length is $\Delta t = t_n - t_{n-1}$. We employ the Backward Euler method for time integration; however, we deviate from the fully implicit rule by replacing the constitutive mobility tensor $\boldsymbol{M}_{\alpha}({}^{n}c_{\alpha})$ by ${}^{n-1}\boldsymbol{M}_{\alpha} := \boldsymbol{M}_{\alpha}({}^{n-1}c_{\alpha})$ for $\alpha = \text{Li,X}$, which infers forward differencing. Hence, we evaluate $\boldsymbol{j}_{\alpha} := {}^{n}\boldsymbol{j}_{\alpha}$ at $t = t_n$ as

$$\boldsymbol{j}_{\alpha}(\boldsymbol{\nabla}\mu'_{\alpha}) = -{}^{n-1}\boldsymbol{M}_{\alpha} \cdot \boldsymbol{\nabla}\mu'_{\alpha} = -{}^{n-1}\boldsymbol{M}_{\alpha} \cdot \boldsymbol{\nabla}\mu_{\alpha} - {}^{n-1}\boldsymbol{\mathcal{L}}_{\alpha} \cdot \boldsymbol{\nabla}\varphi, \quad \alpha = \text{Li,X} \tag{22}$$

As a direct consequence, we evaluate

$$\boldsymbol{i}_{\text{MAX}}(\boldsymbol{\nabla}\mu_{\text{Li}}, \boldsymbol{\nabla}\mu_{\text{X}}, \boldsymbol{\nabla}\varphi) = -{}^{n-1}\boldsymbol{\mathcal{L}}_{\text{Li}} \cdot \boldsymbol{\nabla}\mu_{\text{Li}} - {}^{n-1}\boldsymbol{\mathcal{L}}_{\text{X}} \cdot \boldsymbol{\nabla}\mu_{\text{X}} - \left[{}^{n-1}\boldsymbol{\mathcal{K}}^{\text{eff}} + \frac{1}{\Delta t}\boldsymbol{\mathcal{E}}\right] \cdot \boldsymbol{\nabla}\varphi + \frac{1}{\Delta t}\boldsymbol{\mathcal{E}} \cdot \boldsymbol{\nabla}^{n-1}\varphi \tag{23}$$

Furthermore, we evaluate

$$i_{\mathrm{MAX},n}([[\mu_{\mathrm{Li}}]],[[\varphi]]) = \left\{ \begin{array}{r} -\bar{\mathcal{L}}[[\mu_{\mathrm{Li}}]] - \left[\bar{\mathcal{K}}^{\mathrm{eff}} + \frac{1}{\Delta t}\bar{\mathcal{E}}\right]\left[\varphi^{\mathrm{e}} - \Phi^{-}\right] + \frac{1}{\Delta t}\bar{\mathcal{E}}\left[{}^{n-1}\varphi^{\mathrm{e}} - {}^{n-1}\Phi^{-}\right] \text{ on } \Gamma_{\mathrm{fe}} \\ -\left[\bar{\mathcal{K}}^{\mathrm{eff}} + \frac{1}{\Delta t}\bar{\mathcal{E}}\right]\left[0 - \varphi^{\mathrm{e}}\right] + \frac{1}{\Delta t}\bar{\mathcal{E}}\left[0 - {}^{n-1}\varphi^{\mathrm{e}}\right] \text{ on } \Gamma_{+} \end{array} \right. \tag{24}$$

The relevant solution (and test) spaces for solutions at the updated time t_n are defined as:

$$\hat{\mathbb{U}} = \hat{\mathbb{U}}^0 = \{\boldsymbol{u} \in \mathbb{H}^1(\Omega):\ u_1 = 0 \text{ on } \Gamma_{\mathrm{ext},2} \cup \Gamma_{\mathrm{ext},3}\} \tag{25a}$$

$$\hat{\mathbb{F}} = \hat{\mathbb{F}}^0 = \{\varphi \in \mathbb{H}^1(\Omega_{\mathrm{e}})\} \tag{25b}$$

$$\hat{\mathbb{M}}_{\mathrm{Li}} = \hat{\mathbb{M}}_{\mathrm{Li}}^0 = \{\mu_{\mathrm{Li}} \in \mathbb{L}_2(\Omega_{\mathrm{f}} \cup \Omega_{\mathrm{e}}),\ \mu_{\mathrm{Li}}|_{\Omega_{\mathrm{f}}} = \mathbb{H}^1(\Omega_{\mathrm{f}}),\ \mu_{\mathrm{Li}}|_{\Omega_{\mathrm{e}}} = \mathbb{H}^1(\Omega_{\mathrm{e}})\} \tag{25c}$$

$$\hat{\mathbb{M}}_{\mathrm{X}} = \hat{\mathbb{M}}_{\mathrm{X}}^0 = \{\mu_{\mathrm{X}} \in \mathbb{H}^1(\Omega_{\mathrm{e}})\} \tag{25d}$$

4.2. Potentiostatic problem: Controlling the electric potential $\Phi^{-}(t)$

The most straightforward situation is when the potential value $\Phi^{-}(t)$ (in addition to $\Phi^{+}(t) = 0$) is a prescribed function in time within the negative collector (fibre) domains $\Omega_{\mathrm{f}} := \cup_i \Omega_{\mathrm{f},i}$. The entire problem of solving for the updated fields at $t = t_n$ can now be posed as follows: Find $\boldsymbol{u} \in \hat{\mathbb{U}}$, $\varphi \in \hat{\mathbb{F}}$, $\mu_{\mathrm{Li}} \in \hat{\mathbb{M}}_{\mathrm{Li}}$, $\mu_{\mathrm{X}} \in \hat{\mathbb{M}}_{\mathrm{X}}$, $c_{\mathrm{Li}} \in \mathbb{L}_2(\Omega_{\mathrm{f}} \cup \Omega_{\mathrm{e}})$, and $c_{\mathrm{X}} \in \mathbb{L}_2(\Omega_{\mathrm{e}})$, that solve the set of equations

$$\int_{\Omega_{\mathrm{f}} \cup \Omega_{\mathrm{e}}} \boldsymbol{\sigma} : \boldsymbol{\epsilon}[\delta \boldsymbol{u}] \mathrm{d}V = 0 \qquad \forall \delta \boldsymbol{u} \in \hat{\mathbb{U}}^0 \tag{26a}$$

$$\int_{\Omega_{\mathrm{e}}} \boldsymbol{i}_{\mathrm{MAX}} \cdot \boldsymbol{\nabla}[\delta\varphi] \mathrm{d}V + \int_{\Gamma_{\mathrm{fe}}} i_{\mathrm{Max},n} \delta\varphi \mathrm{d}S - \int_{\Gamma_{+}} i_{\mathrm{Max},n} \delta\varphi \mathrm{d}S = 0 \qquad \forall \delta\varphi \in \hat{\mathbb{F}}^0 \tag{26b}$$

$$\begin{aligned} &-\frac{1}{\Delta t}\int_{\Omega_{\mathrm{f}} \cup \Omega_{\mathrm{e}}} \left[c_{\mathrm{Li}} - {}^{n-1}c_{\mathrm{Li}}\right] \delta\mu_{\mathrm{Li}} \mathrm{d}V + \int_{\Omega_{\mathrm{f}} \cup \Omega_{\mathrm{e}}} \boldsymbol{j}_{\mathrm{Li}} \cdot \boldsymbol{\nabla}[\delta\mu_{\mathrm{Li}}] \mathrm{d}V \\ &+ \int_{\Gamma_{\mathrm{fe}}} j_{\mathrm{Li},n} [[\delta\mu_{\mathrm{Li}}]] \mathrm{d}S - \int_{\Gamma_{+}} j_{\mathrm{Li},n}\, \delta\mu_{\mathrm{Li}} \mathrm{d}S = 0 \qquad \forall \delta\mu_{\mathrm{Li}} \in \hat{\mathbb{M}}_{\mathrm{Li}}^0 \end{aligned} \tag{26c}$$

$$-\frac{1}{\Delta t}\int_{\Omega_{\mathrm{e}}} \left[c_{\mathrm{X}} - {}^{n-1}c_{\mathrm{X}}\right] \delta\mu_{\mathrm{X}} \mathrm{d}V + \int_{\Omega_{\mathrm{e}}} \boldsymbol{j}_{\mathrm{X}} \cdot \boldsymbol{\nabla}[\delta\mu_{\mathrm{X}}] \mathrm{d}V = 0 \qquad \forall \delta\mu_{\mathrm{X}} \in \hat{\mathbb{M}}_{\mathrm{X}}^0 \tag{26d}$$

$$\int_{\Omega_{\mathrm{f}} \cup \Omega_{\mathrm{e}}} \left[\mu_{\mathrm{Li}}^{\mathrm{en}} - \mu_{\mathrm{Li}}\right] \delta c_{\mathrm{Li}} \mathrm{d}V = 0 \qquad \forall \delta c_{\mathrm{Li}} \in \mathbb{L}_2(\Omega_{\mathrm{f}} \cup \Omega_{\mathrm{e}}) \tag{26e}$$

$$\int_{\Omega_{\mathrm{e}}} \left[\mu_{\mathrm{X}}^{\mathrm{en}} - \mu_{\mathrm{X}}\right] \delta c_{\mathrm{X}} \mathrm{d}V = 0 \qquad \forall \delta c_{\mathrm{X}} \in \mathbb{L}_2(\Omega_{\mathrm{e}}) \tag{26f}$$

where the pertinent constitutive relations were given as follows: $\boldsymbol{\sigma}$ is defined in equation (2a) on Ω_{f} and in equation (6a) on Ω_{e}; $\boldsymbol{d}$ is defined in equation (6b) on Ω_{e}; $\boldsymbol{j}_{\mathrm{Li}}$ is defined in equation (2b) on Ω_{f} and in equation (6c) on Ω_{e}; $\boldsymbol{j}_{\mathrm{X}}$ is defined in equation (6e) on Ω_{e}; $\mu_{\mathrm{Li}}^{\mathrm{en}}$ and $\mu_{\mathrm{X}}^{\mathrm{en}}$ are the energetic constitutive expressions of equations (2c), (6d) and (6f), which are given here for completeness:

$$\mu_{\mathrm{Li}}^{\mathrm{en}} = \left\{ \begin{array}{ll} -\zeta\boldsymbol{\alpha} : \boldsymbol{\sigma}(\boldsymbol{\epsilon}, c_{\mathrm{Li}}) + \mu_{\mathrm{Li}}^0 + R\theta_0 \log\left(\frac{\tilde{c}_{\mathrm{Li}}}{1-\tilde{c}_{\mathrm{Li}}}\right) & \text{in } \Omega_{\mathrm{f}} \\ \mu_{\mathrm{Li}}^0 + R\theta_0 \log\left(\tilde{c}_{\mathrm{Li}}\right) & \text{in } \Omega_{\mathrm{e}} \end{array} \right. \tag{27a}$$

$$\mu_{\mathrm{X}}^{\mathrm{en}} = \mu_{\mathrm{X}}^0 + R\theta_0 \log\left(\tilde{c}_{\mathrm{X}}\right) \quad \text{in } \Omega_{\mathrm{e}} \tag{27b}$$

Moreover, $j_{\mathrm{Li},n}$ is defined in equation (10) on Γ_{fe} and in equation (20*a*) on Γ_+. Finally, $\boldsymbol{i}_{\mathrm{MAX}}$ is given in equation (23), whereas $i_{\mathrm{Max},n}$ is defined in equation (24) on Γ_{fe} and Γ_+, respectively.

Remark 3. *We employ a mixed method, since* μ_{Li} *and* μ_{X} *are treated as independent fields in addition to* c_{Li} *and* c_{X}*. This choice requires the additional constraint conditions in equations (26e) and (26f).*

4.3. Galvanostatic problem: Controlling the electric current $I^-(t)$

We consider the problem when the potential value $\Phi^+(t)$ is prescribed (function in time) along the (positive) collector boundary Γ_+, whereas the total current $I^-(t)$ from/to the negative collector (fibre) domains $\Omega_{\mathrm{f}} := \cup_i \Omega_{\mathrm{f},i}$ is assumed to be a known function. The entire problem of solving for the updated fields at $t = t_n$ can now be posed as follows: Find $\boldsymbol{u} \in \hat{\mathbb{U}}$, $\varphi \in \hat{\mathbb{F}}$, $\mu_{\mathrm{Li}} \in \hat{\mathbb{M}}_{\mathrm{Li}}$, $\mu_{\mathrm{X}} \in \hat{\mathbb{M}}_{\mathrm{X}}$, $c_{\mathrm{Li}} \in \mathbb{L}_2(\Omega_{\mathrm{f}} \cup \Omega_{\mathrm{e}})$, $c_{\mathrm{X}} \in \mathbb{L}_2(\Omega_{\mathrm{e}})$, and $\Phi^- \in \mathbb{R}$, that solve the set of equations

$$\int_{\Omega_{\mathrm{f}} \cup \Omega_{\mathrm{e}}} \boldsymbol{\sigma} : \boldsymbol{\epsilon}[\delta \boldsymbol{u}] \mathrm{d}V = 0 \qquad \forall \delta \boldsymbol{u} \in \hat{\mathbb{U}}^0 \tag{28a}$$

$$\int_{\Omega_{\mathrm{e}}} \boldsymbol{i}_{\mathrm{MAX}} \cdot \boldsymbol{\nabla}[\delta\varphi] \mathrm{d}V + \int_{\Gamma_{\mathrm{fe}}} i_{\mathrm{Max},n} \delta\varphi \mathrm{d}S - \int_{\Gamma_+} i_{\mathrm{Max},n} \delta\varphi \mathrm{d}S = 0 \qquad \forall \delta\varphi \in \hat{\mathbb{F}}^0 \tag{28b}$$

$$\begin{aligned} -\frac{1}{\Delta t} \int_{\Omega_{\mathrm{f}} \cup \Omega_{\mathrm{e}}} \left[c_{\mathrm{Li}} - {}^{n-1}c_{\mathrm{Li}}\right] \delta\mu_{\mathrm{Li}} \mathrm{d}V + \int_{\Omega_{\mathrm{f}} \cup \Omega_{\mathrm{e}}} \boldsymbol{j}_{\mathrm{Li}} \cdot \boldsymbol{\nabla}[\delta\mu_{\mathrm{Li}}] \mathrm{d}V \\ + \int_{\Gamma_{\mathrm{fe}}} j_{\mathrm{Li},n} [[\delta\mu_{\mathrm{Li}}]] \mathrm{d}S - \int_{\Gamma_+} j_{\mathrm{Li},n} \delta\mu_{\mathrm{Li}} \mathrm{d}S = 0 \qquad \forall \delta\mu_{\mathrm{Li}} \in \hat{\mathbb{M}}^0_{\mathrm{Li}} \end{aligned} \tag{28c}$$

$$-\frac{1}{\Delta t} \int_{\Omega_{\mathrm{e}}} \left[c_{\mathrm{X}} - {}^{n-1}c_{\mathrm{X}}\right] \delta\mu_{\mathrm{X}} \mathrm{d}V + \int_{\Omega_{\mathrm{e}}} \boldsymbol{j}_{\mathrm{X}} \cdot \boldsymbol{\nabla}[\delta\mu_{\mathrm{X}}] \mathrm{d}V = 0 \qquad \forall \delta\mu_{\mathrm{X}} \in \hat{\mathbb{M}}^0_{\mathrm{X}} \tag{28d}$$

$$\int_{\Omega_{\mathrm{f}} \cup \Omega_{\mathrm{e}}} [\mu^{\mathrm{en}}_{\mathrm{Li}} - \mu_{\mathrm{Li}}] \delta c_{\mathrm{Li}} \mathrm{d}V = 0 \qquad \forall \delta c_{\mathrm{Li}} \in \mathbb{L}_2(\Omega_{\mathrm{f}} \cup \Omega_{\mathrm{e}}) \tag{28e}$$

$$\int_{\Omega_{\mathrm{e}}} [\mu^{\mathrm{en}}_{\mathrm{X}} - \mu_{\mathrm{X}}] \delta c_{\mathrm{X}} \mathrm{d}V = 0 \qquad \forall \delta c_{\mathrm{X}} \in \mathbb{L}_2(\Omega_{\mathrm{e}}) \tag{28f}$$

$$\delta\Phi^- \left[\int_{\Gamma_{\mathrm{fe}}} i_{\mathrm{Max},n} \mathrm{d}S - I^-_{\mathrm{Max}}\right] = 0 \qquad \forall \delta\Phi^- \in \mathbb{R} \tag{28g}$$

Upon comparing with the formulation of the potentiostatic problem, we note that the value of Φ^- is now part of the solution; hence, the additional equation (28*g*) is required.

5. Model specification

5.1. FE-approximation and implementation in COMSOL Multiphysics®

The numerical implementation is done in the commercial FE software COMSOL Multiphysics version 5.4. The Weak form PDE module is used to set-up the time-incremental weak format of the half-cell problem presented in section 4 and the built-in solver MUMPS (MUltifrontal Massively Parallel sparse direct Solver [56]) is used to solve the system of equations. The partial differential equations for the mass and charge balance in the SBE phase (electro-chemical analysis) are discretized with quadratic triangular Lagrange elements. The mass balance in the fibre domains is discretized with cubic triangular Lagrange elements. Finally, the displacement field (linked to the mechanical analysis), in both fibre and SBE domains, are discretized using quartic triangular Lagrange elements. The Fully Coupled Approach available in the COMSOL suite is used to solve the coupled problem which means that the complete system of equations is solved in a monolithic fashion, i.e. without using any staggering between the different physical mechanisms. Moreover, all boundary conditions are applied as Weak Contributions.

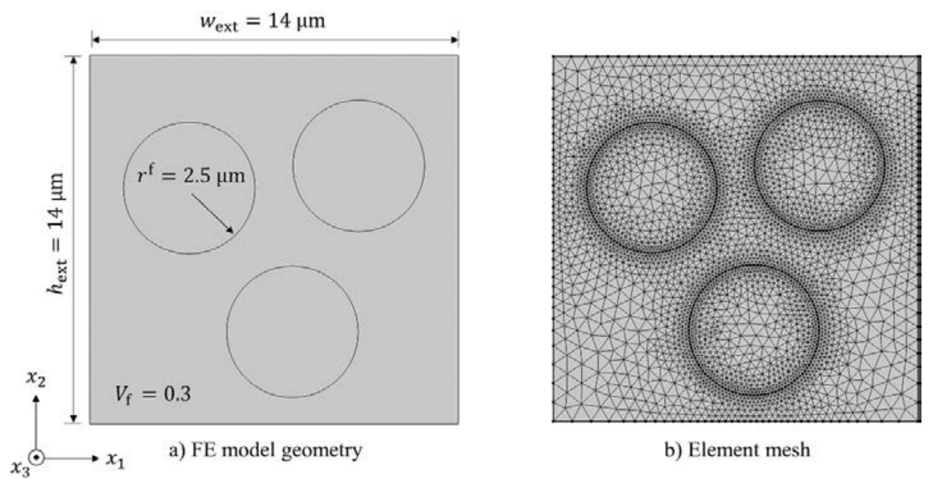

a) FE model geometry

b) Element mesh

Figure 4. (a) Model geometry and (b) triangular element mesh for the FE-model set-up in COMSOL Multiphysics.

5.2. Model geometry and loading conditions

The geometry and element mesh for the chosen two-dimensional FE-model with generic/idealized geometry are illustrated in figure 4. The height (h_{ext}) and width (w_{ext}) are set equal and defined such that the fibre volume fraction is 30% ($V_f = 0.3$). The fibre volume fraction is kept constant (for simplicity) and 30% is selected as a rough estimate based on cross-section images of carbon fibre-SBE electrodes (see figure 3(b)). The fibre distribution in the idealized model is selected arbitrarily. A biased mesh (figure 4(b)) is used with mesh size ranging from 0.1 to 0.6 μm. The mesh size is determined such that the overall solution has converged. It should be noted that local phenomena, such as the deviation from electroneutrality in the immediate vicinity the fibre-SBE interface (see section 6.4), is highly affected by the mesh size. Although the FE-analysis is two-dimensional, it must be kept in mind that the stress state is three-dimensional due to the assumed stress/strain condition in the x_3-direction (along the fibres), see specification below.

The mechanical boundary conditions were given in equations (19*a*) and (19*b*). As to the stress/strain conditions in the x_3-direction, i.e. in the fibre direction (henceforth denoted *loading conditions*), several options are possible. Here, we opt for conditions that simulate those which are typical for beam (and plate) kinematics, whereby the x_3-direction is the beam axis. We then consider the following alternatives:

- **Load(i)**: Standard plane strain, i.e. $\epsilon_{33}(x_1, x_2, t) = \bar{\epsilon}_{33} = 0$. Postprocessing then gives the field $\sigma_{33}(x_1, x_2, t)$ and the normal force $N_{33}(t)$.
- **Load(ii)**: Generalized plane strain, i.e. $\epsilon_{33}(x_1, x_2, t) = \bar{\epsilon}_{33}(t)$ with a prescribed time-variation of $\bar{\epsilon}_{33}(t)$. In order to allow for comparing with experimental data (e.g. from Jacques *et al* [57]), we choose 'ramp-loading' of the form

$$\bar{\epsilon}_{33}(t) = \begin{cases} at, & t \leq t_1 \\ at_1, & t > t_1 \end{cases} \tag{29}$$

  where a is a constant associated with the magnitude of the applied strain and t_1 denotes the time at which no additional strain is applied. Even in this case postprocessing will give the field $\sigma_{33}(x_1, x_2, t)$ and the normal force $N_{33}(t)$.
- **Load(iii)**: Generalized plane stress, defined by $\epsilon_{33}(x_1, x_2, t) = \bar{\epsilon}_{33}(t)$ and the condition

$$N_{33}(t) := \int_{\Omega} \sigma_{33}(\bullet, t) \mathrm{d}S = 0 \tag{30}$$

  where we note that Ω defines a surface in 2D. This is the extra condition that is needed to compute $\bar{\epsilon}_{33}(t)$ as part of the FE-problem. Clearly, postprocessing will provide the field $\sigma_{33}(x_1, x_2, t)$.

5.3. Material parameters

All parameters are homogeneous within the fibres and the SBE, respectively. The complete set of parameter values used in the analysis is listed in table A2. The mobility of Li in the fibres is estimated based on the longitudinal diffusion coefficient for sized IMS65 carbon fibres at $\tilde{c}_{Li} = 0.05$ reported by Kjell *et al* [58] according to the relation $\eta = \frac{D}{R\theta}$, where η is the mobility coefficient and D the measured diffusion coefficient, see Salvadori *et al* [43]. Moreover, the mobility coefficients for Li and X in the SBE are chosen equal and the values are approximated as $\eta_{\mathrm{Li}} = \eta_{\mathrm{X}} = \frac{\mathcal{K}^{\mathrm{eff}}}{F^2[z_{\mathrm{Li}}^2 c_{\mathrm{Li,ref}} + z_{\mathrm{X}}^2 c_{\mathrm{X,ref}}]}$ (in accordance with Chintapalli *et al* [59]), where $\mathcal{K}^{\mathrm{eff}}$ is the measured ion conductivity of the SBE reported by Ihrner *et al* [19], and $c_{\mathrm{Li,ref}} = c_{\mathrm{X,ref}} = 1000$ mol m^{-3} corresponds to the initial salt concentration in the SBE.

The reference/standard value of μ for Li in the fibres is based on measurements by Kjell *et al* [58] as $\mu_{\mathrm{Li}}^0 = \frac{1}{2} F U_{\mathrm{eq}}(\tilde{c}_{\mathrm{Li}} = 0.05)$, while $\mu_{\mathrm{Li}}^0 = 0$ in the electrolyte. The specific capacity of the carbon fibres (C^{f}) is defined based on measurements on negative half-cells (carbon fibres in liquid electrolyte) by Jacques *et al* [60]. The selected capacity is reported for lithiation with a current rate corresponding to approximately one hour discharge time. The maximum Li-concentration in the fibres is defined based on the specific capacity according to: $c_{\mathrm{Li,max}} = C^{\mathrm{f}} \rho^{\mathrm{f}} 3600/F$. The coefficients of the insertion tensor $\boldsymbol{\alpha}^{\mathrm{ch}}$ are based on measurements by Jacques *et al* [60] for the corresponding current. The mobility resistances linked to the mass flux and current flow at the fibre-electrolyte and Li-metal-electrolyte interfaces are approximated as: $\bar{M} = i_0/[R\theta_0 F]$ (assuming small overpotential). For simplicity, we assume that the exchange current density (denoted i_0) is constant. We also assume that the interface resistance associated with permittivity can be expressed as $\bar{\mathcal{E}} = \varepsilon/\delta$, where δ is the assumed thickness of the electric double layer. The relative permittivity is assumed equal to $\varepsilon_r = 10$ based on previous work on polyether electrolytes (Fontanella and Wintersgill [61]) in accordance with Ganser *et al* [35]. The thickness of the electric double layer is set to 0.5 nm, see [35, 62].

6. Results and discussion

6.1. Electro-chemical cycling: Galvanostatic vs. potentiostatic control

To demonstrate the characteristics of the two basic controls of electro-chemical cycling, the studied structural battery half-cell is discharged (i.e. the fibres are being lithiated) under galvanostatic conditions (figure 5) and potentiostatic conditions (figure 6), while assuming the loading condition Load(iii) (generalized plane stress). The results are derived by solving the weak form of the governing equations described in section 4. Hence, two-way coupling between the electro-chemical and mechanical fields is utilized (i.e. the system is solved with full interaction). The cell potential (Φ^-) and current (I^-) during the two different discharge processes are presented in figures 5(b) and 6(b).

For the galvanostatic control (figure 5), the battery cell is discharged at a constant current $I^-(t) = I^{\mathrm{pre}}$, estimated as: $I^{\mathrm{pre}} = C^{\mathrm{f}} m^{\mathrm{f}}$, where C^{f} is the assumed specific capacity for the fibre and m^{f} is the mass per unit length of the fibres. During the discharge process the current remains constant while the cell potential drops. A stopping criterion is defined as $\max_{\boldsymbol{x} \in \Omega_{\mathrm{f}}} \tilde{c}_{\mathrm{Li}}(\boldsymbol{x}) = 1$, which corresponds to $\Phi^- \approx 0.25$ V. At this moment it is assumed that the cell is fully discharged, i.e. that the fibres are assumed to be fully lithiated. It should be noted that the stopping condition is based on $\tilde{c}_{\mathrm{Li}}$ (in the fibres), rather than on Φ^-. This is due to the non-linear characteristics of the variation in equilibrium potential (see equation (15)) as $\tilde{c}_{\mathrm{Li}}$ in the fibres approaches 1. The time for the battery cell to be fully discharged under the given conditions turns out to be approximately 3580 s, which is less than the nominally expected 1 h.

Compared with experimental data reported by Kjell *et al* [58] and Johannisson *et al* [18], the overall behaviour of the potential $\Phi^-(t)$ during galvanostic discharge, as shown in figure 5(b), is in agreement (given the expected deviation linked to the simplified expression for the activity coefficient of the fibres).

Figures 5(c)–(f) show the normalized Li-concentration $\tilde{c}_{\mathrm{Li}}$ and the strain field $\epsilon_{11}(x_1, x_2, t)$ at the two time instances $t_1 = 1000$ s and $t_2 = 2500$ s. Since the fibres expand with increasing c_{Li}, strains build up inside the material (see equation(4*a*)) during the discharge process (compare ε_{11} in figures 5(d) and (f)).

For the potentiostatic control (figure 6), the potential remains constant while the current drops. In this case the potential is predefined as $\Phi^-(t) = \Phi^{\mathrm{pre}} = 0.05$ V. For simplicity the same stopping criterion (as for the galvanostatic case) is used. The current density at which this limit is reached is approximately 0.55 A m^{-2}. Under these conditions the discharge time is 450 s. The reason for the relatively short discharge time (compared with the galvanostatic discharge process) is the fact that the current density is controlled by the applied potential and the assumed variation of the equilibrium potential (see equation (15)). Hence, under the given conditions the current density is larger during the entire discharge process compared with the galvanostatic case.

The normalized Li-concentration $\tilde{c}_{\mathrm{Li}}$ and the strain field $\epsilon_{11}(x_1, x_2, t)$ at the two time instances $t_1 = 100$ s and $t_2 = 300$ s are presented in figures 6(c)–(f). In comparison with the galvanostatic control, a more pronounced variation in the Li-concentration in the fibres and the SBE is observed. Moreover, in the beginning of the discharge process (i.e. for low c_{Li} in the fibres) the current density is much larger compared with later in the process. This is problematic from the viewpoint of electric power losses, mass transport limitations, etc. The mechanical strains are found to develop similarly during galvanostatic and

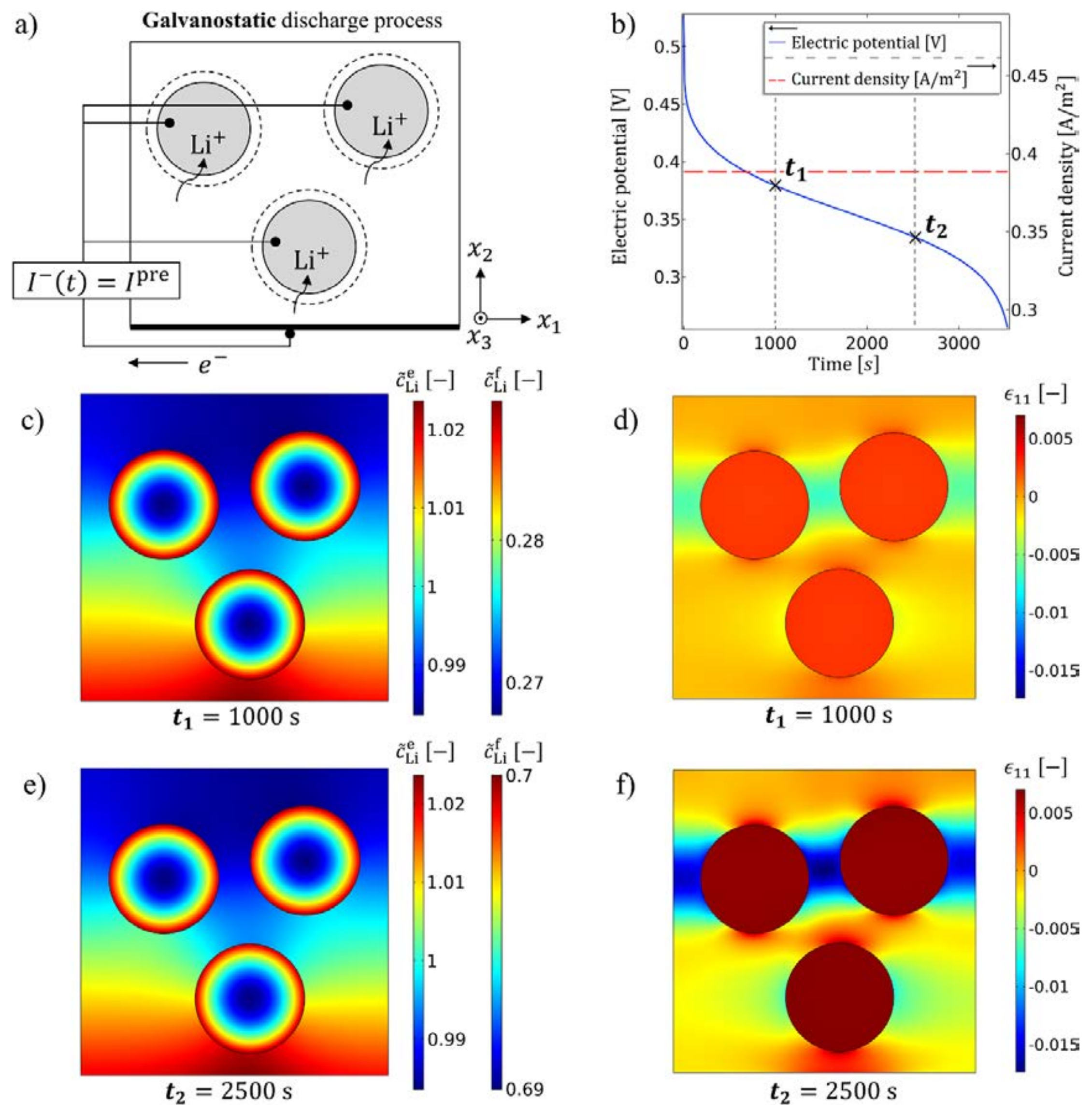

Figure 5. (a) **Galvanostatic** discharge process, whereby the current is controlled: $I^-(t) = I^{\text{pre}}$. (b) Cell potential (Φ^-) and current (I^-) versus time. (c)–(f) Normalized Li-concentration $\tilde{c}_{\text{Li}}$ and strain field $\epsilon_{11}(x_1, x_2, t)$ at two different time instances. Superscripts e and f denote electrolyte and fibre, respectively.

potentiostatic discharge processes. Note, however, that the strains develop at rates associated with the set electric loading conditions.

It should be noted that the utilized electrical interface condition (equation (13)) can be expressed as the linearized form of the classical Butler–Volmer equation (see equation (17)). The exponential term $\frac{F\overline{\eta}}{R\theta_0}$ in equation(17) is equal to 0.39 in the galvanostatic case and varies (with the current density) between 4.5 and 2.6 for the potentiostatic case. This means that the validity of the linearization (associated with the assumption of small overpotentials) of the Butler–Volmer equation [28] is violated for the large current densities present during the beginning of the potentiostatic discharge process. For the galvanostatic case, the introduced error/deviation (compared with the standard form of the Butler–Volmer equation in equation (17)) is on the third decimal (i.e. is considered negligible).

6.2. Assessment of coupling between electro-chemical and mechanical fields

The electro-chemo-mechanical coupling effects will be assessed in the proposed framework as follows:

- **Coup(i)**: One-way coupling: The electro-chemical problem solved independently and the result (concentration field) is used as input data for the solution of the mechanical problem. Achieved by setting $\Lambda = 0$, where the parameter $\Lambda := \zeta \boldsymbol{\alpha}^{\text{ch}} : \boldsymbol{\sigma}$ is a measure of the coupling strength.
- **Coup(ii)**: Two-way coupling: The system is solved with full interaction.

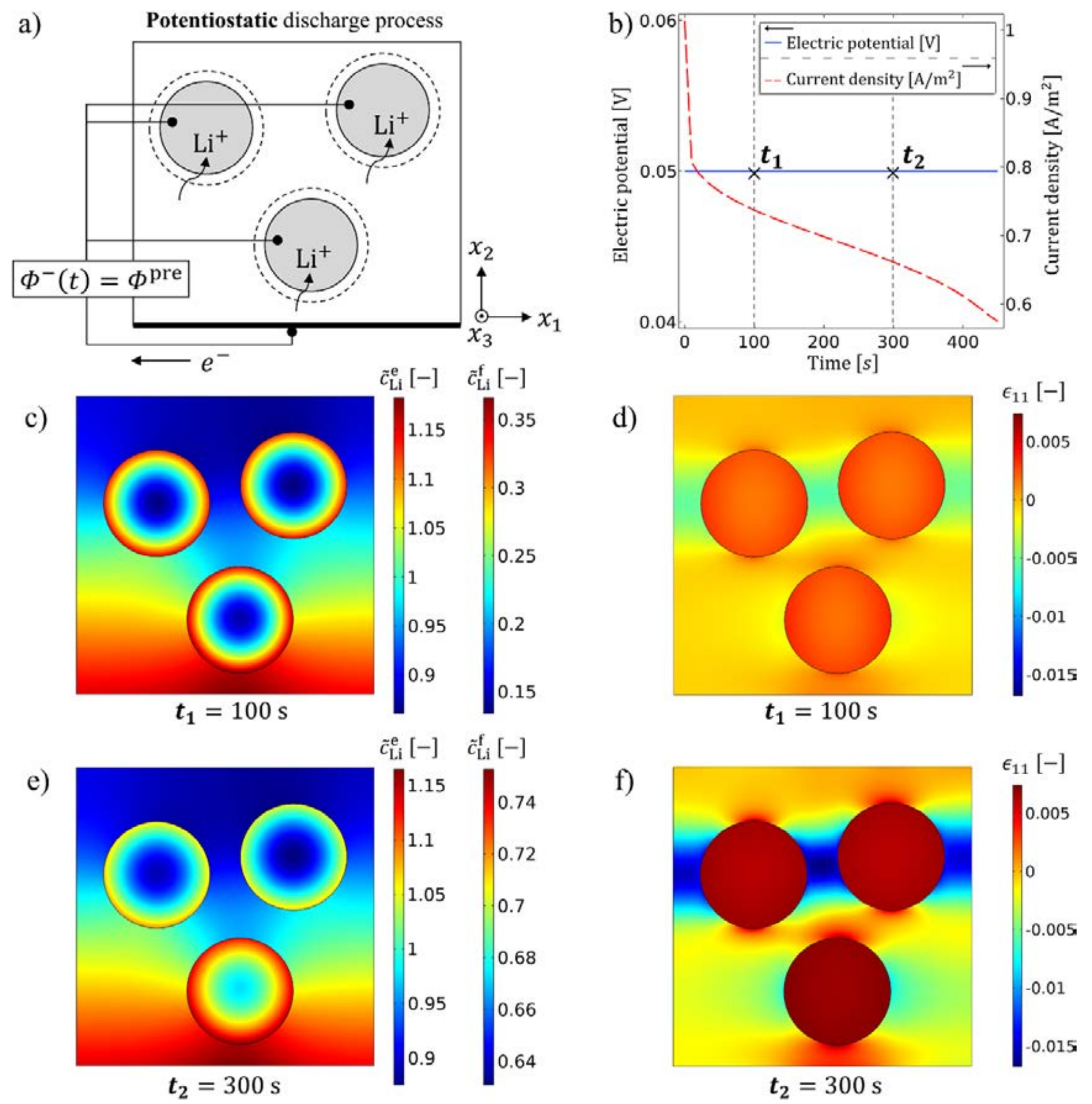

Figure 6. (a) **Potentiostatic** discharge process, whereby the potential is controlled: $\Phi^-(t) = \Phi^{\rm pre}$. (b) Cell potential ($\Phi^-$) and current ($I^-$) versus time. (c)–(f) Normalized Li-concentration $\tilde{c}_{\rm Li}$ and strain field $\epsilon_{11}(x_1, x_2, t)$ at two different time instances. Superscripts e and f denote electrolyte and fibre, respectively.

The computational results are obtained while considering a single discharge cycle, assuming the loading condition Load(iii) (generalized plane stress condition), and adopting galvanostatic control. How the electric potential Φ^- varies with time is shown in figure 7 for the two cases of (de)coupling as defined above. It appears that the difference in $\Phi^-(t)$ between Coup(i) and Coup(ii) increases with time due to the change in stress state as fibres expand with increasing $c_{\rm Li}$.

Due to the fact that the coefficients of $\boldsymbol{\alpha}^{\rm ch}$ increase with reduced (dis)charge current (as reported by Jacques *et al* [60]), this coupling effect will be more pronounced for lower (dis)charge currents.

6.3. Assessment of out-of-plane loading conditions

The out-of-plane loading conditions are assessed by studying the three loading cases presented in section 5.2 (illustrated in figure 8(a)). The computational results in figures 8 are obtained while considering a single discharge cycle, assuming full electro-chemo-mechanical coupling and adopting galvanostatic control. For Load(ii), the prescribed strain is set to $\varepsilon_{33} = 0.01$ and is applied at the initial time step. The stress field $\sigma_{33}(x_1, x_2, t)$ is shown in figures 8(d)–(f). Clearly, the axial stress field depends significantly on the chosen loading condition. As expected, the magnitude of σ_{33} is much smaller for Load(iii), for which the axial load vanishes. The difference in σ_{33} is translated to the value of Λ, which affects the transport properties. This fact is manifested in the shift of the transient part of $\Phi^-(t)$, as shown in figures 8(b)–(c). Hence, the shift in potential depends on the assumed parameters associated with Λ. This means that the elastic properties of the constituents and mechanical loading/boundary conditions strongly affect the electro-chemical performance.

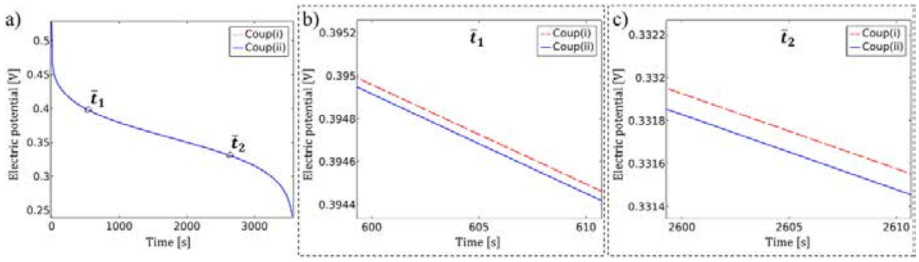

Figure 7. (a) Time variation of the electric potential Φ^- during galvanostatic discharging for the two cases Coup(i): one-way coupling, $\Lambda = 0$ and Coup(ii): two-way coupling. (b)–(c) Zoom-in of the fibre potential at the two times $\bar{t}_1 \in [600 : 610]$ s and $\bar{t}_2 \in [2600 : 2610]$ s, respectively.

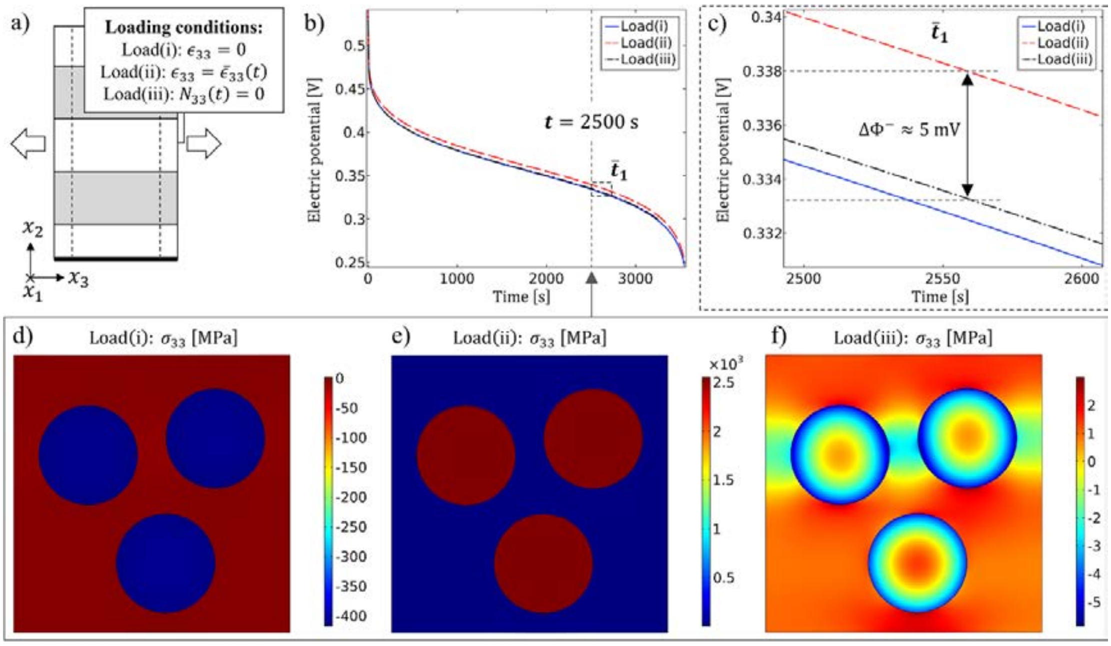

Figure 8. (a) External (mechanical) loading conditions in x_3-direction. For Load(ii), the prescribed strain is set to $\varepsilon_{33} = 0.01$ and is applied at the initial time step. (b) Time-variation of the electric potential Φ^- during the discharge process. (c) Zoom-in of the electric potential at the time $\bar{t}_1 \in [2500 : 2600]$ s. (d)–(f) Snapshots of stress fields $\sigma_{33}(x_1, x_2, t)$ at $t = 2500$ s for the three different loading conditions Load(i), Load(ii), Load(iii).

Compared with experimental data reported by Jacques *et al* [57], the shift in $\Phi^-(t)$ due to applied mechanical strain is in the same order of magnitude. Jacques *et al* [57] reported a shift in electric potential for a carbon fibre half-cell (in liquid electrolyte) of +4.5 mV for a mechanical strain of 0.6% applied in the fibre direction. The estimated shift in $\Phi^-(t)$ using the developed framework is approximately +5 mV for a mechanical strain of 1% as presented in figure 8(c).

It should be noted that the studied half-cell corresponds to a regular battery cell (i.e. a full-cell), but where one of the electrodes is replaced with Li-metal (as reference). Hence, the predicted results for the half-cell are expected to correlate with the effects on the complete structural battery (i.e. the full-cell illustrated in figure 1(b)). For example, the predicted shift in the electric potential (figures 8(b)–(c)) will also occur in the complete structural battery as the cell potential is simply the potential difference between the electrodes.

In all components made from structural batteries the insertion induced expansion and deformation of the cell will be constrained. Loading conditions 1 and 3 (i.e. Load(i) and Load(iii)) represent the extreme cases of constrained vs. unconstrained conditions. In order to determine which of these loading conditions that occur in service it is necessary to analyse the complete macrostructure of the laminated battery cells.

6.4. Assessment of electroneutrality

The total (free) charge in the electrolyte is

$$\gamma = z'_{\mathrm{Li}} c_{\mathrm{Li}} + z'_{\mathrm{X}} c_{\mathrm{X}} = F[c_{\mathrm{Li}} - c_{\mathrm{X}}] \tag{31}$$

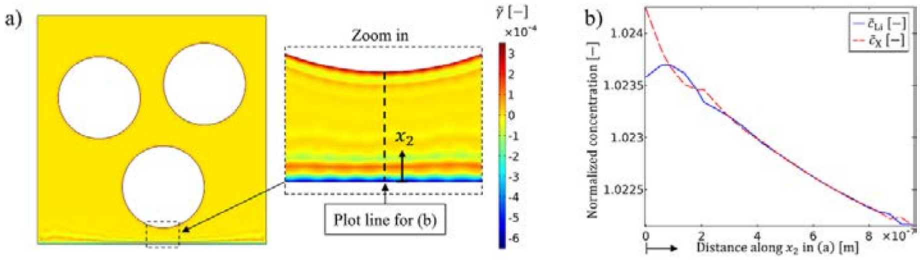

Figure 9. (a) Normalized free charge ($\hat{\gamma}$) in the electrolyte at $t = 1000$ s for Load(iii) and galvanostatic discharging. (b) Normalized concentrations $\tilde{c}_{\mathrm{Li}}$ and $\tilde{c}_{\mathrm{X}}$ plotted along the plot line in (a).

where we used that the valence numbers are $z_{\mathrm{Li}} = +1$ and $z_{\mathrm{X}} = -1$. A very frequent assumption in the electrochemical literature on conventional Li-batteries, used as an *a priori* constraint, is that $\gamma = 0$. Such an electroneutrality assumption would thus infer that $c_{\mathrm{Li}} = c_{\mathrm{X}}$. In order to have an objective measure of the deviation from electroneutrality, we introduced the normalized (with respect to Li) charge

$$\tilde{\gamma} = \frac{\gamma}{z'_{\mathrm{Li}} c_{\mathrm{Li}}} = 1 - \frac{c_{\mathrm{X}}}{c_{\mathrm{Li}}} \tag{32}$$

Figure 9(a) shows the field $\tilde{\gamma}$ in the electrolyte domain at the time $t = 1000$ s for the loading case Load(iii) and galvanostatic discharging. The individual fields c_{Li} and c_{X} are presented in figure 9(b). Since it can be concluded from the computational result that $|\tilde{\gamma}| \leq 6 \cdot 10^{-4}$, the (pre)assumption of electroneutrality would have been justified; however, close to the interfaces (e.g. fibre-electrolyte) the discrepancy between c_{Li} and c_{X} is more visible, which has also been observed in the literature, e.g. Ganser *et al* [35].

7. Conclusions and Outlook to future work

In this paper we present a thermodynamically consistent modelling approach for studying the electro-chemo-mechanical properties of structural batteries. The laminated architecture is studied, and restriction is made to a so called half-cell. While the SBE is considered isotropic on the studied geometric scale, the strongly anisotropic (transverse isotropy) character of the fibres is taken into account. The proposed modelling framework accounts for stress-assisted transport in addition to standard diffusion and migration.

We demonstrate that the framework can be used to simulate the galvanostatic and potentiostatic charge/discharge conditions of structural batteries. Further, the numerical studies reveal that it is vital to account for two-way coupling between the mechanical and electro-chemical processes. In the case of generalized plane stress conditions (when the magnitude of the out-of-plane stresses is small), the coupling effects have minor influence on the electro-chemical performance. However, in the case of severely constrained deformation (such as plane strain) or applied mechanical loading, then the coupling effects become more pronounced. Hence, for structural batteries that are intended to carry mechanical load it becomes crucial to account for the coupled effects.

As to future development, it is desirable to refine some of the model assumptions. For example, a more refined expression for the activity coefficient of the fibres is desirable. In this work a simplified expression is used which results in some discrepancy between the numerical prediction and experimental data [18, 58] for the time variation of the electric potential of the studied half-cell. Moreover, previous studies on conventional lithium ion batteries have shown that the thickness of the electrodes has a significant effect on the electrical performance [63–65]. Due to the inferior transport properties of the constituents in the structural battery [19, 20, 58], as compared with a conventional battery, the performance is expected to be highly affected by the electrode dimensions. Evaluation of such effects will be the subject of future work. Finally, the provided framework can be used for evaluating the performance of the complete structural battery by adding the separator phase and the positive electrode. To realize this, procedures for dealing with the electrode coating in the positive electrode need to be developed. This will also be the scope of future work.

Acknowledgment

This project has been funded by the European Union, Clean Sky Joint Undertaking 2, Horizon 2020 under Grant Agreement Number 738085 and USAF, contract FA9550-17-1-0338, which are gratefully acknowledged.

Table A1. List of symbols.

Symbol	Unit	Description
φ	[V]	Electrical potential
μ_α	[J mol^{-1}]	Chemical potential of species α
c_α	[mol m^{-3}]	Mass concentration (molarity) of species α
$\tilde{c}_\alpha$	[-]	Normalized mass concentration of species α
$\boldsymbol{\sigma}$	[Pa]	Stress tensor
E	[Pa]	Elasticity tensor
$\boldsymbol{u}$	[m]	Displacement field tensor
$\boldsymbol{\epsilon}$	[-]	Strain tensor
$\boldsymbol{\epsilon}^{\text{ch}}$	[-]	Lithium insertion strain
$\boldsymbol{\alpha}^{\text{ch}}$	[-]	Insertion tensor
$\boldsymbol{j}_\alpha$	[mol m^{-2}s^{-1}]	Mass flux vector
η_α	[m^{2}mol s^{-1}J^{-1}]	Mobility coefficient of species α
$\boldsymbol{M}_\alpha$	[mol^2 m^{-1}s^{-1}J^{-1}]	Mobility tensor for species α
$\boldsymbol{\mathcal{L}}_\alpha$	[A mol m^{-1}J^{-1}]	Electric mobility ($\boldsymbol{\mathcal{L}}_\alpha = z'_\alpha \boldsymbol{M}_\alpha$)
$\boldsymbol{\mathcal{K}}^{\text{eff}}$	[S m^{-1}]	Effective conductivity ($\boldsymbol{\mathcal{K}}^{\text{eff}} = [z'_{\text{Li}}]^2 \boldsymbol{M}_{\text{Li}} + [z'_{\text{X}}]^2 \boldsymbol{M}_{\text{X}}$)
$\boldsymbol{\mathcal{E}}$	[F m^{-1}]	Permittivity tensor
$\bar{M}$	[mol^2 m^{-2}s^{-1}J^{-1}]	Interface mobility
$\bar{\mathcal{L}}$	[A mol m^{-2}J^{-1}]	Interface electric mobility ($\bar{\mathcal{L}} = z'_{\text{Li}} \bar{M}$)
$\bar{\mathcal{K}}^{\text{eff}}$	[S m^{-2}]	Interface effective conductivity ($\bar{\mathcal{K}}^{\text{eff}} = [z'_{\text{Li}}]^2 \bar{M}$)
$\bar{\mathcal{E}}$	[F m^{-2}]	Interface permittivity
C	[Ah kg^{-1}]	Specific capacity
$\boldsymbol{i}_{e-}$	[A m^{-2}]	Electron current density
$\boldsymbol{i}_{\text{ions}}$	[A m^{-2}]	Ion current density
$\boldsymbol{i}_{\text{Max}}$	[A m^{-2}]	Maxwell current
$\boldsymbol{d}$	[C m^{-2}]	Electric flux density vector
θ	[K]	Temperature
ε	[F m^{-1}]	Permittivity
ζ	[m^3 mol^{-1}]	Inverse of maximum Li-concentration in fibre ($\zeta = c_{\text{Li,max}}^{-1}$)
L	[Pa]	Lame's first parameter
G	[Pa]	Shear modulus
E	[Pa]	Young's modulus
ν	[-]	Poisson's ratio
ρ	[g cm^{-3}]	Density
D	[m^2 s^{-1}]	Diffusion coefficient
U_{eq}	[V]	Equilibrium potential
Φ^+	[V]	Positive electrode potential (set to 0)
Φ^-	[V]	Negative electrode (fibre) potential, controlled or computed
I^-	[A]	Circuit current (fibre), controlled or computed
$\boldsymbol{\sigma}_n$	[Pa]	Traction
z	[-]	Valence number
z'	[C mol^{-1}]	Specific charge, $z' = Fz$
$\bar{S}$	[V^{-1}]	Resistance coefficient, $\bar{S} = \frac{F}{R\theta_0}$
$\bar{\eta}$	[V]	Surface overpotential
δ	[m]	Thickness of electric double layer
t	[s]	Time
Λ	[J mol^{-1}]	Coupling strength parameter ($\Lambda = \zeta \boldsymbol{\alpha}^{\text{ch}} : \boldsymbol{\sigma}$)
γ	[C m^{-3}]	Total (free) charge in electrolyte
$\tilde{\gamma}$	[-]	Normalized (with respect to Li) charge in electrolyte
Ω	[-]	Domain
Γ	[-]	Boundary

Table A2. Parameters used in the analysis. Superscripts e and f denote electrolyte and fibre, respectively.

Parameter	Value	Unit	Description	Reference
$E^{f}_{\|}$	294	[GPa]	Longitudinal (L) modulus fibre	[58, 66]
$E^{f}_{\perp}$	22	[GPa]	Transverse (T) modulus fibre	[66]
$G^{f}_{\|}$	12.5	[GPa]	Shear modulus fibre (LT)	[66]
$\nu^{f}_{\perp}, \nu^{f}_{\|}$	0.2, 0.2	[-]	Poisson's ratio fibre	[66]
E^{e}	0.535	[GPa]	Young's modulus SBE	[19, 20]
ν^{e}	0.38	[-]	Poisson's ratio SBE	-
η^{e}_{Li}	$1.07 \cdot 10^{-15}$	$[\mathrm{m^2 mol\, s^{-1} J^{-1}}]$	Mobility of Li^+ in SBE (based on ion conductivity)	[19]
η^{e}_{X}	$1.07 \cdot 10^{-15}$	$[\mathrm{m^2 mol\, s^{-1} J^{-1}}]$	Mobility of X^- in SBE (based on ion conductivity)	[19]
η^{f}_{Li}	$5.8 \cdot 10^{-18}$	$[\mathrm{m^2 mol\, s^{-1} J^{-1}}]$	Mobility of Li^+ in fibre (based on diffusion coefficient)	[58]
C^{f}	168	$[\mathrm{Ah\, kg^{-1}}]$	Specific capacity of carbon fibre (1 h lithiation)	[60]
$\alpha^{ch}_{\perp}$	0.01	[-]	Transverse Li insertion expansion coefficient (1 h)	[60]
$\alpha^{ch}_{\|}$	0.002	[-]	Longitudinal Li insertion expansion coefficient (1 h)	[60]
$c^{f}_{\mathrm{Li,ini}}$	10	$[\mathrm{mol\, m^{-3}}]$	Initial Li concentration fibre	-
$c^{f}_{\mathrm{Li,max}}$	11 596	$[\mathrm{mol\, m^{-3}}]$	Maximum Li concentration fibre (based on C^{f})	-
$c^{e}_{\alpha,\mathrm{ini}}$	1000	$[\mathrm{mol\, m^{-3}}]$	Initial Li^+ and X^- concentration SBE	[19, 20]
$c^{e}_{\alpha,\mathrm{ref}}$	1000	$[\mathrm{mol\, m^{-3}}]$	Reference concentration of Li^+ and X^- in the SBE	-
θ_0	293.15	[K]	Reference temperature	-
ε_0	$8.854 \cdot 10^{-12}$	$[\mathrm{F\, m^{-1}}]$	Vacuum permittivity	-
ε_r	10	[-]	Relative permittivity	[35, 61]
i_0	1	$[\mathrm{A\, m^{-2}}]$	Exchange current density	[58]
$\mu^{0,f}_{\mathrm{Li}}$	$3.86 \cdot 10^{4}$	$[\mathrm{J\, mol^{-1}}]$	Reference chemical potential Li in fibre (vs. Li/Li^+)	[58]
$\mu^{0,e}_{\alpha}$	0	$[\mathrm{J\, mol^{-1}}]$	Reference chemical potential Li^+ and X^- in SBE	-
f^{e}_{α}	1	[-]	Activity coefficient Li^+ and X^- in SBE	-
r^{f}	$2.5 \cdot 10^{-6}$	[m]	Fibre radius	-
ρ^{f}	1.85	$[\mathrm{g\, cm^{-3}}]$	Fibre density	-
δ	$0.5 \cdot 10^{-9}$	[m]	Thickness of electric double layer	[35, 62]
F	96 485	$[\mathrm{C\, mol^{-1}}]$	Faraday's constant	-
R	8.314	$[\mathrm{J\, K^{-1} mol^{-1}}]$	Gas constant	-

Appendix A. Symbols and parameters

Symbols and parameters used in the analysis presented in this paper are listed in tables A1 and A2. Moreover, the explicit representation of the elasticity tensor $\mathbf{E}$ (for transverse isotropy) in Voigt matrix notation is defined as

$$\mathbf{E} = \begin{bmatrix} L_\perp + 2G_\perp & L_\perp & L_\| & 0 & 0 & 0 \\ L_\perp & L_\perp + 2G_\perp & L_\| & 0 & 0 & 0 \\ L_\| & L_\| & L_\| + 2G_\| & 0 & 0 & 0 \\ 0 & 0 & 0 & G_\perp & 0 & 0 \\ 0 & 0 & 0 & 0 & G_\| & 0 \\ 0 & 0 & 0 & 0 & 0 & G_\| \end{bmatrix} \tag{A1}$$

where $L_\perp = \frac{E_\perp \nu_\perp}{(1+\nu_\perp)(1-2\nu_\perp)}$ and $L_\| = \frac{E_\| \nu_\|}{(1+\nu_\|)(1-2\nu_\|)}$.

ORCID iDs

David Carlstedt https://orcid.org/0000-0002-7867-3745
Leif E Asp https://orcid.org/0000-0003-0630-2037

References

[1] Asp L E *et al* 2019 Structural battery composites: a review *Funct. Composites Struct.* **1** 042001

[2] Lendlein A and Trask R S 2018 Multifunctional materials: concepts, function-structure relationships, knowledge-based design, translational materials research *Multi-functional Mater.* **1** 010201

[3] Thomas J P and Qidwai M A 2004 Mechanical design and performance of composite multifunctional materials *Acta Mater.* **52** 2155–64

[4] Liu P, Sherman E and Jacobsen A 2009 Design and fabrication of multifunctional structural batteries *J. Power Sources* **189** 646–50

[5] Gibson R F 2010 A review of recent research on mechanics of multifunctional composite materials and structures *Compos. Struct.* **92** 2793–2810
[6] González C, Vilatela J J, Molina-Aldareguía J M, Lopes C S and LLorca J 2017 Structural composites for multifunctional applications: current challenges and future trends *Prog. Mater. Sci.* **89** 194–251
[7] Adam T J, Liao G, Petersen J, Geier S, Finke B, Wierach P, Kwade A and Wiedemann M 2018 Multifunctional composites for future energy storage in aerospace structures *Energies* **11** 335
[8] Ladpli P, Nardari R, Kopsaftopoulos F and Chang F K 2019 Multifunctional energy storage composite structures with embedded lithium-ion batteries *J. Power Sources* **414** 517–29
[9] Moyer K, Meng C, Marshall B, Assal O, Eaves J, Perez D, Karkkainen R, Roberson L and Pint C L 2020 Carbon fiber reinforced structural lithium-ion battery composite: Multifunctional power integration for cubesats *Energy Storage Mater.* **24** 676–81
[10] Zhao Y, Zhao D, Zhang T, Li H, Zhang B and Zhenchong Z 2020 Preparation and multifunctional performance of carbon fiber-reinforced plastic composites for laminated structural batteries *Polym. Compos.* **41** 1–11
[11] Carlstedt D and Asp L E 2020 Performance analysis framework for structural battery composites in electric vehicles *Composite* B **186** 107822
[12] Asp L E and Greenhalgh E S 2014 Structural power composites *Compos. Sci. Technol.* **101** 41–61
[13] Wetzel E D 2004 Reducing weight: Multifunctional composites integrated power, communications and structure *AMPTIAC Q* **8** 91–5
[14] Snyder J F, Gienger E B and Wetzel E D 2015 Performance metrics for structural composites with electrochemical multifunctionality *J. Compos. Mater.* **49** 1835–48
[15] Johannisson W, Zenkert D and Lindbergh G 2019 Model of a structural battery and its potential for system level mass savings *Multifunct. Mater.* **2** 035002
[16] Ekstedt S, Wysocki M and Asp L E 2010 Structural batteries made from fibre reinforced composites *Plastics Rubber Composites* **39** 148–50
[17] Carlson T 2013 Multifunctional composite materials—design, manufacture and experimental characterisation *Doctoral Thesis* Luleå University of Technology, Luleå, Sweden (http://www.diva-portal.org/smash/get/diva2:999197/FULLTEXT01.pdf)
[18] Johannisson W, Ihrner N, Zenkert D, Johansson M, Carlstedt D, Asp L E and Sieland F 2018 Multifunctional performance of a carbon fiber UD lamina electrode for structural batteries *Compos. Sci. Technol.* **168** 81–87
[19] Ihrner N, Johannisson W, Sieland F, Zenkert D and Johansson M 2017 Structural lithium ion battery electrolytes: Via reaction induced phase-separation *J. Mater. Chem.* A **5** 25652–9
[20] Schneider L M, Ihrner N, Zenkert D and Johansson M 2019 Bicontinuous electrolytes via thermally initiated polymerization for structural lithium ion batteries *ACS Appl. Energy Mater.* **2** 4362–9
[21] Fredi G *et al* 2018 Graphitic microstructure and performance of carbon fibre Li-ion structural battery electrodes *Multifunct. Mater.* **1** 015003
[22] Kjell M H, Jacques E, Zenkert D, Behm M and Lindbergh G 2011 PAN-based carbon fiber negative electrodes for structural lithiumion battery *J. Electrochem. Soc.* **158** A1455–60
[23] Hagberg J, Maples H, Alvim K, Xu J, Johannisson W, Bismarck A, Zenkert D and Lindbergh G 2018 Lithium iron phosphate coated carbon fiber electrodes for structural lithium ion batteries *Compos. Sci. Technol.* **162** 235–43
[24] Xu K 2004 Nonaqueous liquid electrolytes for lithium-based rechargeable batteries *Chem. Rev.* **104** 4303–4417
[25] Newman J and Tiedemann W 1975 Porous electrode theory with battery applications *AIChE J.* **21** 25–41
[26] Doyle M, Fuller T F and Newman J 1993 Modeling of galvanostatic charge and discharge of the lithium/polymer/insertion cell *J. Electrochem. Soc.* **140** 1526
[27] Doyle M and Newman J 1995 The use of mathematical modeling in the design of lithium/polymer battery systems *Electrochim. Acta* **40** 2191–6
[28] Newman J and Thomas-Alyea K E 2004 *Electrochem. Syst.* (Wiley: The ECS series of texts and monographs)
[29] Purkayastha R T and McMeeking R M 2012 An integrated 2-D model of a lithium ion battery : The effect of material parameters and morphology on storage particle stress *Computat. Mech.* **50** 209–27
[30] Grazioli D, Magri M and Salvadori A 2016 Computational modeling of Li-ion batteries *Computat. Mech.* **58** 889–909
[31] Grazioli D, Zadin V, Brandell D and Simone A 2019 Electrochemical-mechanical modeling of solid polymer electrolytes: Stress development and non-uniform electric current density in trench geometry microbatteries *Electrochim. Acta* **296** 1142–62
[32] Grazioli D, Verners O, Zadin V, Brandell D and Simone A 2019 Electrochemical-mechanical modeling of solid polymer electrolytes: Impact of mechanical stresses on Li-ion battery performance *Electrochim. Acta* **296** 1122–41
[33] Bucci G, Chiang Y M and Carter W C 2016 Formulation of the coupled electrochemical-mechanical boundary value problem, with applications to transport of multiple charged species *Acta Mater.* **104** 33–51
[34] Wu B and Lu W 2017 A battery model that fully couples mechanics and electrochemistry at both particle and electrode levels by incorporation of particle interaction *J. Power Sources* **360** 360–72
[35] Ganser M, Hildebrand F E, Kamlah M and McMeeking R M 2019 A finite strain electro-chemo-mechanical theory for ion transport with application to binary/solid electrolytes *J. Mech. Phys. Solids* **125** 681–713
[36] Ganser M *et al* 2019 An extended formulation of Butler-Volmer electrochemical reaction kinetics including the influence of mechanics *J. Electrochem. Soc.* **166** H167–H176
[37] Xu R, Yang Y, Yin F, Liu P, Cloetens P, Liu Y, Lin F and Zhao K 2019 Heterogeneous damage in Li-ion batteries: Experimental analysis and theoretical modeling *J. Mech. Phys. Solids* **129** 160–83
[38] Wan T H and Ciucci F 2020 Electro-chemo-mechanical modeling of solid-state batteries *Electrochim. Acta* **331** 135355
[39] Bower A F, Guduru P R and Sethuraman V A 2011 A finite strain model of stress, diffusion, plastic flow and electrochemical reactions in a lithium-ion half-cell *J. Mech. Phys. Solids* **59** 804–28
[40] Wu B and Lu W 2019 A consistently coupled multiscale mechanical – electrochemical battery model with particle interaction and its validation *J. Mech. Phys. Solids* **125** 89–111
[41] Salvadori A, Bosco E and Grazioli D 2014 A computational homogenization approach for Li-ion battery cells: Part 1 - Formulation *J. Mech. Phys. Solids* **65** 114–37
[42] Salvadori A, Grazioli D and Geers M G D 2015 Governing equations for a two-scale analysis of Li-ion battery cells *Int. J. Solids Struct.* **59** 90–109
[43] Salvadori A, Grazioli D, Geers M G D, Danilov D and Notten P H L 2015 A multiscale-compatible approach in modeling ionic transport in the electrolyte of (Lithium ion) batteries *J. Power Sources* **293** 892–911

[44] Salvadori A, Mcmeeking R, Grazioli D and Magri M 2018 A coupled model of transport-reaction-mechanics with trapping. Part I – Small strain analysis *J. Mech. Phys. Solids* **114** 1–30

[45] Xu R and Zhao K 2016 Electrochemomechanics of electrodes in Li-ion batteries: A review *J. Electrochem. Energy Convers. Storage* **13** 030803

[46] Zhao Y, Stein P, Bai Y, Al-siraj M, Yang Y and Xu B 2019 A review on modeling of electro-chemo-mechanics in lithium-ion batteries *J. Power Sources* **413** 259–83

[47] Carlstedt D, Marklund E and Asp L E 2019 Effects of state of charge on elastic properties of 3D structural battery composites *Compos. Sci. Technol.* **169** 26–33

[48] Carlstedt D and Asp L E 2019 Thermal and diffusion induced stresses in a structural battery under galvanostatic cycling *Compos. Sci. Technol.* **179** 69–78

[49] Xu J, Lindbergh G and Varna J 2018 Carbon fiber composites with battery function: Stresses and dimensional changes due to Li-ion diffusion *J. Compos. Mater.* **52** 2729–42

[50] Xu J, Lindbergh G and Varna J 2018 Multiphysics modeling of mechanical and electrochemical phenomena in structural composites for energy storage: Single carbon fiber micro-battery *J. Reinf. Plast. Compos.* **37** 701–15

[51] Leijonmarck S, Carlson T, Lindbergh G, Asp L E, Maples H and Bismarck A 2013 Solid polymer electrolyte-coated carbon fibres for structural and novel micro batteries *Compos. Sci. Technol.* **89** 149–57

[52] Tu V, Asp L E, Shirsova N, Larsson F, Runesson K and Jäanicke R 2020 Performance of bicontinuous structural electrolytes *Multifunct. Mater.* **3** 025001

[53] Dionisi F, Harnden R and Zenkert D 2017 A model to analyse deformations and stresses in structural batteries due to electrode expansions *Compos. Struct.* **179** 580–9

[54] Johannisson W, Harnden R, Zenkert D and Lindbergh G 2020 Shape-morphing carbon fiber composite using electrochemical actuation *Proc. Natl Acad. Sci.* **117** 7658–64

[55] Bazant M Z 2014 II. Equilibrium thermodynamics lecture 8: The nernst equation. lecture notes in 10.626 electrochemical energy systems. Massachusetts Institute of Technology: Mit open course ware (available at: https://ocw.mit.edu/courses/chemical-engineering/10-626-electrochemical-energy-systems-spring-2014/lecture-notes/MIT10_626S14_S11lec08.pdf)

[56] Multifrontal massively parallel solver (mumps 4.8.4) user's guide 2008 (available at: http://mumps.enseeiht.fr/doc/userguide_4.8.4.pdf)

[57] Jacques E, Kjell M H, Zenkert D and Lindbergh G 2013 Piezo-electrochemical effect in lithium-intercalated carbon fibres *Electrochem. Commun.* **35** 65–7

[58] Kjell M H, Zavalis T G, Behm M and Lindbergh G 2013 Electrochemical characterization of lithium intercalation processes of PAN-based carbon fibers in a microelectrode system *J. Electrochem. Soc.* **160** A1473–81

[59] Chintapalli M, Timachova K, Olson K R, Mecham S J, Devaux D, DeSimone J M and Balsara N P 2016 Relationship between conductivity, ion diffusion and transference number in perfluoropolyether electrolytes *Macromolecules* **49** 3508–15

[60] Jacques E, Hellqvist Kjell M, Zenkert D, Lindbergh G and Behm M 2013 Expansion of carbon fibres induced by lithium intercalation for structural electrode applications *Carbon* **59** 246–54

[61] Fontanella J J and Wintersgill M C 1989 Low frequency dielectric properties of polyether electrolytes low frequency dielectric properties of polyether Electrolytes *Polymer Electrolyte Reviews-2* **2** MacCallum J R and Vincent C A (London and New York: Elsevier Applied Science) 43–60

[62] Braun S, Yada C and Latz A 2015 Thermodynamically consistent model for space-charge-layer formation in a solid electrolyte *J. Phys. Chem.* C **119** 22281–8

[63] Zheng H, Li J, Song X, Liu G and Battaglia V S 2012 A comprehensive understanding of electrode thickness effects on the electrochemical performances of Li-ion battery cathodes *Electrochim. Acta* **71** 258–65

[64] Singh M, Kaiser J and Hahn H 2015 Thick electrodes for high energy lithium ion batteries *J. Electrochem. Soc.* **162** A1196–A1201

[65] Danner T, Singh M, Hein S, Kaiser J, Hahn H and Latz A 2016 Thick electrodes for Li-ion batteries: A model based analysis *J. Power Sources* **334** 191–201

[66] Duan S, Liu F, Pettersson T, Creighton C and Asp L E 2020 Determination of transverse and shear moduli of single carbon fibres *Carbon* **158** 772–82